

## Research Paper

# Anti-cancer immune priming with $\beta$ -radioligand therapy using a novel high affinity antibody selectively targeting the 4Ig-Isoform of B7-H3

Sarah E. Glazer<sup>1#</sup>, Margie N. Sutton<sup>1#</sup>, Ping Yang<sup>1</sup>, Federica Pisaneschi<sup>1</sup>, Manu Sebastian<sup>2</sup>, Seth T. Gammon<sup>1✉</sup>, David Piwnica-Worms<sup>1✉</sup>

1. Department of Cancer Systems Imaging, University of Texas MD Anderson Cancer Center, Houston, TX, USA.

2. Department of Veterinary Medicine & Surgery, University of Texas MD Anderson Cancer Center, Houston, TX, USA.

# Co-first authors.

✉ Corresponding authors: 1881 East Road, Unit 1907 Houston, TX 77054. Email addresses: dpiwnica-worms@mdanderson.org; stgammon@mdanderson.org.

© The author(s). This is an open access article distributed under the terms of the Creative Commons Attribution License (<https://creativecommons.org/licenses/by/4.0/>). See <https://ivyspring.com/terms> for full terms and conditions.

Received: 2025.08.07; Accepted: 2026.01.13; Published: 2026.03.12

## Abstract

**Rationale:** Radioligand therapy (RLT) is an emerging oncologic strategy that uses molecularly targeted therapeutic radioisotopes to reduce tumor burden and improve survival in patients with advanced cancers. Expanding RLT to new targets and understanding its systemic immune effects could enhance its clinical impact. B7-H3 (CD276) is an attractive target due to its high differential expression in solid tumors compared to normal tissues. However, the presence of two isoforms, 4Ig-B7-H3 (tumor-associated) and 2Ig-B7-H3 (soluble decoy), poses challenges for selective targeting, especially in the context of RLT.

**Methods:** A novel IgG2a monoclonal antibody (MIL33B) was developed with high affinity for 4Ig-B7-H3 (72 picomolar) and 8- to 18-fold selectivity over soluble 2Ig-B7-H3. Target specificity was assessed using live-cell fluorescence microscopy with AF594-labeled MIL33B. *In vivo* tumor binding was evaluated by PET-CT imaging with <sup>89</sup>Zr-labeled MIL33B in murine xenograft (HeLa cervical) and syngeneic tumor models (4T1 breast, B16F10 melanoma, CT26 colorectal) expressing human 4Ig-B7-H3. Therapeutic efficacy was tested using <sup>90</sup>Y-labeled MIL33B (100  $\mu$ Ci) in an established CT26 colorectal tumor model. Immunologic effects were analyzed to assess CD8<sup>+</sup> T-cell activation and immune memory.

**Results:** MIL33B demonstrated strong membranous localization using live cell fluorescence microscopy. PET-CT imaging with <sup>89</sup>Zr-labeled MIL33B confirmed robust tumor-selective binding *in vivo*. A single systemic dose of <sup>90</sup>Y-MIL33B achieved 53% long-term survival in a 4Ig-B7-H3-dependent manner in an otherwise fatal CT26 colorectal syngeneic tumor model. Immunologic analysis revealed that <sup>90</sup>Y-MIL33B RLT acted as an immune priming event, engaging CD8<sup>+</sup> T-cell activation and inducing immunological memory.

**Conclusions:** MIL33B enables selective targeting of 4Ig-B7-H3 for beta-emitting RLT, overcoming challenges posed by soluble isoforms. These findings support further investigation of MIL33B as a systemic therapeutic with immune-priming potential, either alone or in combination strategies for cancer treatment.

## Introduction

Radiotheranostics, also referred to as radioligand therapy (RLT), functions as a systemic modality designed to eradicate primary tumors, disseminated metastases, and occult micrometastatic disease through targeted delivery of cytotoxic radiation (**Figure 1A**) [1]. By comparison, conventional external beam radiation therapy (EBRT) targets with curative intent a defined radiation field localized to the

primary tumor, and in some applications, to oligometastatic disease [2], but many patients present with distant macro- and micro-metastases and continuously shed detectable levels of circulating tumor cells into the systemic circulation outside the radiation field [2]. Both RLT and EBRT are conventionally thought to achieve their effect through direct radiation-induced toxicity to the tumor cell

compartment via irreparable DNA damage; however, standard EBRT has been shown to evoke complex immune responses, with evidence for both immune activating (abscopal effect) and immune suppressive actions [2-4]. Mechanistically, RLT induces tumor cell death via localized generation of radiation-induced reactive oxygen species (ROS), single/double DNA strand breaks, and oxidative stress, with collateral effects on the TIME [1, 5-7]. Despite clinical successes, the narrow spectrum of FDA-approved targets and the opportunity for enhanced understanding of mechanisms of action of RLT portend an unmet medical need to expand the repertoire of second-generation targets and high-affinity ligands.

In this regard, B7-H3 (CD276), a homologue of the B7 superfamily of cell-surface immune co-regulatory proteins, is found in a wide variety of cancers (colon, renal, cervical, esophageal, hepatocellular, neuroblastoma, breast, pancreatic, prostate, head and neck, glioblastoma, ovarian, and NSCLC, among others) [8-16], correlating with poor prognosis, reduced survival, and increased metastasis [17]. While *B7-H3* mRNA is readily detected in most human tissues, by contrast, B7-H3 protein expression is tightly regulated by microRNAs, particularly miR-29, leading to significant differential protein expression between tumors and normal tissues [18]. B7-H3 protein is present in only a subset of normal cells and tissues, such as placenta and testis, wherein the extracellular domain of B7-H3 would be poorly accessible to a targeting agent in the blood [19, 20]. Compared to other radioligand therapy targets, such as PSMA or HER2, which exhibit antigen densities of  $\sim 5 \times 10^5$  to  $10^6$  molecules/cell [21, 22], B7-H3 expression on solid tumors is widespread, but more heterogeneous. Some tumor types, such as breast and lung cancers, show modest expression ( $\sim 10^4$  to  $5 \times 10^5$  molecules/cell) [23], while others, such as neuroblastoma and prostate cancer [24, 25], show high level expression of B7-H3. Furthermore, B7-H3 protein can be induced on multiple components of the TIME (cancer cells, cancer-associated vasculature, neutrophils, monocytes, dendritic cells and other antigen-presenting cells [8,26-33]), and thus, the combination of tumor/tumor-associated selective expression with minimal normal tissue expression portend a favorable therapeutic index, attracting interest as an oncologic target, including for RLT [8, 33-36] (Figure 1B).

Importantly, human B7-H3 is a type 1 transmembrane protein expressed in two isoforms, a 4Ig-B7-H3 isoform consisting of an extracellular ectodomain comprising two pairs of immunoglobulin constant and variable domains (IgC/IgV, IgC/IgV) [26, 37-39], and a 2Ig-B7-H3 isoform containing only

one extracellular IgC/IgV pair (Figure 1C) [40]. This stands in contrast to rodents, wherein only the 2Ig isoform is expressed [39], and may be responsible for the species-specific differential roles of B7-H3 in regulating immune checkpoint observed in early studies [41]. In humans, a soluble component (s2Ig-B7-H3), likely representing ectodomain shedding of B7-H3, similar to other type 1 and 2 membrane proteins and members of the B7 family [42, 43], has been identified and accumulates in compartments outside the TIME, such as the blood pool and cerebral spinal fluid [44-46]. Increased circulating s2Ig-B7-H3 has been identified in the serum of patients during progression of malignancies and inflammatory states [47-51]. This is of particular concern in the context of imaging agent and low-mass RLT therapeutic development because s2Ig-B7-H3 can act as a decoy target and ligand sink, potentially diminishing efficacy and increasing toxicities of ligands that target both isoforms. None-the-less, abundant evidence indicates that 4Ig-B7-H3 is the dominant isoform present on the cell surface of human cancers [26, 37-39, 52], and unique to B7 family members, the presence of 4Ig and 2Ig isoforms may provide a “handle” to develop a 4Ig-tumor-selective ligand, such as an antibody, for RLT to overcome challenges presented by circulating B7 isoforms.

Herein, a novel targeted beta-radioligand antibody therapeutic with 8- to 18-fold selectivity for the 4Ig isoform of B7-H3 compared to the 2Ig isoform was extensively validated *in vitro* and *in vivo*, yielding functional cures in syngeneic immunocompetent murine tumor models. The biochemical B7-H3 targeting mechanism was firmly established, and the high cure rate in a syngeneic model opened the opportunity to study systemic immune responses and long-term anti-tumor memory. Mechanistically, 4Ig-B7-H3-targeted beta-RLT functioned as a primary immune priming event shown to promote downstream CD8<sup>+</sup> T-cell activation and induce immunological memory *in vivo*, thus experimentally reinforcing the concept that targeted beta-RLT ultimately engages systemic adaptive immunity.

## Materials & Brief Methods

See **Supplementary Materials** for detailed methods.

### Antibody Development and MIL33B Production

The MDACC Monoclonal Antibody Core Facility (protocol 00000620-RN01 through RN03) was utilized to develop anti-B7-H3 monoclonal antibodies. Briefly, mouse L cells transfected using polybrene with a lentivirus containing the *homo sapiens* CD276

transcript variant 1 mRNA (NM\_001024736.1) (Genecopia LPP-Z3060-LV105-100) and puromycin suppression was used for selection. New Zealand White mice (NZBWF1/J, Jackson Laboratory) or Balb/c (Charles River) were immunized with the cells by foot-pad immunization [133]. Sera obtained from immunized mice were screened for differential binding to human 4Ig-B7-H3-expressing or vector control transcript (Genecopia LPP-NEG-Lv105-025-c) and parental cells as well as binding to mouse 2Ig-B7-H3 protein (R&D 1397-B3-050) by ELISA. Selected clones were used to generate stable hybridomas. Monoclonal antibodies obtained from the supernatants of these hybridomas were further evaluated for human, mouse and porcine 4Ig-/2Ig-B7-H3 affinity and specificity.

MIL33B was purified from supernatants from the MIL33B hybridoma by either the MDACC Monoclonal Antibody Core or by BioXCell. ELISA was used to validate the affinity of each MIL33B stock for human and mouse 4Ig-/2Ig-B7-H3.

### ELISA and Bi-Layer Interferometry Analysis

ELISA was performed using MIL33B to probe plate-bound human and mouse B7-H3 extracellular domains (human 4Ig-B7-H3 protein R&D 2318-B3-050; mouse 2Ig-B7-H3 protein R&D 1397-B3-050), with 1:2000 dilutions of secondary antibody, (goat anti-mouse IgG (Fc) HRP (Biorad)). OCTET RED384 platform, a technology based on Bio-Layer Interferometry (BLI) was utilized to further characterize antibodies and their binding kinetics. Briefly, the murine-derived anti-B7-H3 clone, MIL33B, was immobilized on AMC biosensors using anti-mouse IgG Fc capture at a fixed concentration of 10 µg/ml. Loaded biosensors were subsequently interacted with 7 serial dilutions (ranging from 3 nM to 200 nM) of the extracellular domain of various B7-H3 isoforms or relevant B7 protein homologues. Association and dissociation constants,  $K_a$  and  $K_d$ , respectively, and calculated affinity constants ( $K_D$ ) were measured using Octet Analysis Studio 13.

### Human Tissue Microarray Fluorescence Staining

Frozen human tissue microarrays were purchased from Fisher Scientific (50-180-886) containing arrayed normal and cancer tissues for multiple organ sites. Staining was performed following a brief fix (5 minutes) at room temperature of the slide in 4% paraformaldehyde. Following fixation, slides were washed two times in 5% BSA/PBS for 5 minutes each. Blocking was performed in 5% BSA/PBS containing 1:100 IgG2a (Final concentration ~ 50 µg/mL) at room temperature

for 30 minutes. Primary antibody was added in 1% BSA/PBS and incubated overnight at 4°C protected from light. MIL33B-AF594 and IgG2a-AF594 were diluted 1:100; final concentration was 10 µg/mL. Following overnight incubation, slides were washed 2X in 1% BSA/PBS for 5 minutes each. Nuclear staining was performed with DAPI at a dilution of 1:1000 in 1% BSA/PBS for 10 minutes at room temperature. Slides were washed an additional time in 1% BSA/PBS and mounted using antifade mounting media. Once dried, the slides were sealed and images were captured on a Nikon TiE Epifluorescence microscope.

### Cell Line Generation

B16F10 murine melanoma cells, 4T1 murine triple negative breast cancer cells, and CT26 murine colorectal carcinoma cells were transfected using polybrene with lentiviral constructs containing the *homo sapien CD276* transcript variant 1 mRNA (NM\_001024736.1) (Genecopia LPP-Z3060-LV105-100) or the negative vector control transcript (Genecopia LPP-NEG-Lv105-025-c) and selected in puromycin. CD276<sup>-/-</sup> cells were generated by transfecting HeLa parental cells with human-derived CD276 CRISPR/Cas9 pooled plasmids (Santa Cruz Biotechnology sc-402032) or double nickase control plasmids (each containing a GFP marker, three separate guide RNAs, and a plasmid encoding Cas9). GFP-positive cells were sorted and expanded. HCT116 cells or HCT116 cells stably transfected with a *KB5-IkBα-FLUC* reporter [134] were cultured as described.

### Live Cell Fluorescence Microscopy

Cells were plated in a 4-well Ibidi dish at  $5 \times 10^4$  cells in 500 µL of media. Cells were incubated at 37 °C in 5% CO<sub>2</sub> for 24-48 hours. MIL33B or mouse isotype control IgG2a (BioXcell BE0085) were labeled with Alexa594 (ThermoFisher A20185) by the MDACC flow cytometry core. Subsequently, cells were incubated with 10 µg/mL of either Alexa549-labeled MIL33B or IgG2a and 5 µL of a 1:100 dilution in PBS of Hoechst stain for 1 hour and imaged on a Nikon TiE inverted microscope (40x objective).

### Antibody Conjugation with p-SCN-Bn-Deferoxamine or p-SCN-Bn-DOTA

For antibodies conjugated with p-SCN-Bn-Deferoxamine (MacroCyclics), 4-7 mg/mL of either MIL33B or mouse IgG2a (BioXcell) were desalted into 0.1M NaHCO<sub>3</sub> (pH = 8.4) using 7K MWCO Zeba (ThermoFisher) protein desalting spin columns. When conjugating MIL33B to p-SCN-Bn-DOTA (MacroCyclics), the stock solution

was concentrated to 9-11 mg /mL using Amicon Ultra-0.5 centrifugal filter units with a 30 kDa cutoff, and then similarly desalted into a 0.1 M solution of sodium bicarbonate (pH = 8.4). 5 mg of each respective chelator dissolved in DMSO were incubated with the respective antibodies for 1 hour at 37°C with periodic mixing. Final antibodies were desalted into 0.1 M ammonium acetate (pH = 6.6-7) as described previously [135].

### Radiolabeling of MIL33B with Zirconium-89

The MDACC cyclotron facility or the University of Wisconsin cyclotron facility produced Zirconium-89 in 1 M oxalic acid. Zirconium-89 oxalate (3 mCi) was neutralized to pH 7 by 1.0 M Na<sub>2</sub>CO<sub>3</sub> (pH = 11). Following, 20-30 µL of a 4-7 mg/mL solution of DFO-conjugated antibodies, MIL33B or mouse IgG2a, was added to the buffer and the final volume brought to 200 µL with PBS and with zirconium-89 oxalate for 1 hour at 37 °C. Chelation efficiency was evaluated by radio-TLC with antibody solutions quenched in 50 mM DPTA (pH = 7) using 50 mM DPTA (pH = 7) as the running solvent. A PD-10 column was used to purify chelated antibodies into PBS. Radio-TLC with antibody solutions quenched in 50 mM DPTA pH 7 and with 50 mM DPTA pH 7 as the running solvent was used to determine chelation efficiency. Purity was validated by radio-TLC and radio-SEC-HPLC with a 200 10-30 Superdex column (71 minute isocratic elution in PBS with 0.1 M NaCl and 0.05% sodium azide). <sup>89</sup>Zr-labeled antibodies were assessed for stability at room temperature in PBS and evaluated at 4 hours, 24 hours and 72 hours after radiolabeling by radio-SEC-HPLC.

### Radiolabeling of MIL33B with Yttrium-90

[<sup>90</sup>Y]YCl<sub>3</sub> in 0.04 M HCl was purchased from Eckert & Ziegler Radiopharma. [<sup>90</sup>Y]Yttrium chloride was buffered in an equal volume of 0.1 M ammonium acetate (pH = 5.6). Following, 50 µL of DOTA-MIL33B was added to the solution. DOTA-MIL33B was incubated with [<sup>90</sup>Y]yttrium chloride for 1 hour at 37°C. Chelation efficiency was evaluated by radio-TLC with antibody solutions quenched in 50 mM EDTA using 10 mM EDTA as the running solvent. <sup>90</sup>Y-DOTA-MIL33B were purified into PBS using a PD-10 column. Purity was validated by radio-TLC and radio-SEC-HPLC with a 200 10-30 Superdex column (71 minute isocratic elution in PBS with 0.1 M NaCl and 0.05% sodium azide). The stability of <sup>90</sup>Y-DOTA-MIL33B incubated at room temperature in PBS was evaluated at 4 hours, 24 hours and 48 hours after radiolabeling by radio-SEC-HPLC.

### Tumor Models

All experiments were approved under an MDACC IACUC protocol (00001179-RN01 and RN02). Mice aged 5-12 weeks were used for all experiments. Tumor cells were implanted subcutaneously on the flanks of female athymic nude immunodeficient mice strain 490 (Charles River) or flanks of respective immunocompetent female Balb/c mice (Taconic) or female C57BL/6 mice (Taconic). For all mice, tumors were measured using calipers twice weekly. Mice were defined to reach endpoint when either the length or width of the tumor reached 15 mm or the tumors had ulcers of 3 mm, at which point mice were euthanized by CO<sub>2</sub> asphyxiation and cervical dislocation.

### PET-CT Imaging Methods and Analysis

Mice were injected with approximately 20-60 µCi of either <sup>89</sup>Zr-DFO-MIL33B or <sup>89</sup>Zr-DFO-IgG2a intravenously. For cold blocking experiments, mice received 200 µg of un-labeled MIL33B 1 hour before injection with the tracer of interest. Mice were imaged at 24 hours, 72 hours and 144 hours on a PET-CT scanner (Albira, Bruker), with a field of view of 120 mm for PET and 70-75 mm for CT. Mice were imaged with a single 10 minute PET scan and a fast CT HV, HD scan. VOIs were drawn in PMOD and used to calculate %ID/cc for respective VOIs at each time point.

### Cherenkov Radiation Optical Imaging

Images of mice were obtained using an IVIS Spectrum, open filter, FOV 23 cm x 23 cm, and image acquisition time of 5 minutes, followed by acquisition of a bright light image.

### <sup>90</sup>Y-DOTA-MIL33B Treatment Strategy

Mice harboring CT26 4Ig-B7-H3 or neg vector tumors were selected for tumors with a volume of about 50 mm<sup>3</sup> - 150 mm<sup>3</sup> at 10-12 days post tumor implantation and randomized into treatment groups. Untreated mice were followed regardless of initial tumor size. Mice were treated with intravenous injection of 100 µCi of <sup>90</sup>Y-DOTA-MIL33B or 100 µL of sterile saline. For HeLa B7-H3<sup>+/+</sup> WT or HeLa B7-H3<sup>-/-</sup> KO, 5x10<sup>6</sup> cells were implanted subcutaneously in the flanks of athymic nude mice. Mice harboring HeLa B7-H3<sup>+/+</sup> or HeLa B7-H3<sup>-/-</sup> KO tumors were not size selected and received an intravenous injection of 100 µCi of <sup>90</sup>Y-DOTA-MIL33B 30 days post tumor implantation or were not treated (serving as a tumor growth rate control), thus anchoring survival with previously performed animal studies [59].

## Tumor Growth Rate Comparison

In comparing the growth rates of HeLa B7-H3<sup>+/+</sup> WT or HeLa B7-H3<sup>-/-</sup> KO tumors treated with <sup>90</sup>Y-DOTA-MIL33B i.v., changes in tumor growth were calculated on a mouse by mouse basis by calculating the change in tumor size at each time point compared to initial tumor size (**Figure S10**). Slopes of tumor growth (growth rates) were calculated with a 3-point exponential fitting curve using Prism software.

## Immune Cell Depletion *In Vivo*

Mice harboring CT26 4Ig-B7-H3 tumors were treated with a single dose of 100  $\mu$ Ci of <sup>90</sup>Y-DOTA-MIL33B i.v.; 1 day before treatment, mice received either 250  $\mu$ g of anti-mouse CD8b (clone 53-5.8 BioXcell), anti-mouse CD4 (clone GK1.5 BioXcell), or anti-rat IgG polyclonal (BioXcell) i.p. and then received subsequent doses of each respective depleting antibody 2 days, 6 days and 9 days post treatment with <sup>90</sup>Y-DOTA-MIL33B i.v. Response to treatment with depleting antibodies was monitored by caliper measurements of the tumors.

## Tumor Cell Re-Challenge

Mice harboring CT26 4Ig-B7-H3 tumors that had previously been treated with 100  $\mu$ Ci of <sup>90</sup>Y-DOTA-MIL33B were followed for 100 days post tumor implantation. Mice whose tumors had regressed and did not recur at the 100-day time point were deemed long-term survivors. Long-term survivors were implanted with 5x10<sup>4</sup> CT26 4Ig-B7-H3 or CT26 neg vector control cells in 100  $\mu$ L of a 1:1 ratio of PBS:matrigel subcutaneously on the left flank. Age-matched naïve female Balb/c mice (Taconic Biosciences) were also implanted identically with 5x10<sup>4</sup> CT26 4Ig-B7-H3 or CT26 neg vector control cells in 100  $\mu$ L of a 1:1 ratio of PBS:matrigel subcutaneously on the left flank. Response to the tumor cell re-challenge was monitored by caliper measurements.

## MIL33B Monotherapy

Balb/c female mice (Taconic) were implanted with 1x10<sup>5</sup> CT26 4Ig-B7-H3 cells in 100  $\mu$ L PBS subcutaneously in the right flank. Mice received 200  $\mu$ g i.p. of either MIL33B, mouse IgG2a isotype control antibody (BioXcell), or 100  $\mu$ L PBS on day 3, 6, 9, 12, 15, 18, 21, and 24 post cell implantation.

## Histology

Mice harboring CT26 4Ig-B7-H3 tumors were treated with 100  $\mu$ Ci of <sup>90</sup>Y-DOTA-MIL33B i.v. according to the protocol. 6 days after treatment, mice were sacrificed, tumors fixed in formalin for 24-36 hours and then subsequently stored in 70% ethanol

for radioactive decay. Tumors were stained by H&E staining, anti-CD4 (Abcam ab183685), anti-CD3 (Cell Signaling 99940), anti-CD8 (Abcam ab217344), anti-Ki67 (Cell Signaling 12202), anti-CD31 (Abcam ab124432) and anti-cleaved caspase-3 (Cell Signaling 9662) by the MDACC histology core facility. Histopathology review, including immunohistochemistry scoring, was performed by a board-certified pathologist.

## Multiplexed Immunofluorescence Staining

Multiplexed Immunofluorescence (mIF) staining was performed on tissues collected and processed as previously described (Histology section). Using the established Lunaphore COMET system, FFPE tissues were placed in tanks containing BioGenex EZ Elegans AR2 buffer, enclosed inside a BioGenex EZ Retriever microwave system. The samples were heated in the microwave to 107°C for 15 minutes to dewax, rehydrate and retrieve the antigens. After heating, the slides were cooled to room temperature and loaded into the COMET system where they were covered and sealed by a fast-fluidic exchange microfluidics chip for staining and imaging in the instrument. Cycle temperature remained at 37°C for the duration of the staining, incubation time was 16 minutes for primary and 4 minutes for secondary antibodies, and image capture was obtained at exposure times of 25 ms, 250 ms or 400 ms. The following antibodies were used at the given dilutions below: Cycle 1: CD8 (Bethyl, BLR173J, Channel: Cy5, Dilution: 1:100) Cycle 2: CD4 (CST, D7D27, Chanel: Tritc, Dilution1:100); Cycle 3: TCF1/TCF7 (CST, C63D9, Channel: Cy5, Dilution: 1:100); Cycle 4: B7-H3 (R&D, AF1397, Channel: Cy5, Dilution: 1:200). COMET collected images in OME-Tiff formats, which were scanned and visualized in Comet Viewer (Lunaphore). Image analysis was performed using Oncotopix Discovery (Visiopharm, v.2023.01).

## RNA sequencing and Single Cell RNA-Seq

CT26 4Ig-B7-H3 and CT26 negative vector cells were seeded at 70% confluency for 24 hours before RNA isolation was performed using QIAGEN RNA isolation kit (Kit #74104). Purified RNA underwent quality control and then the Poly(A) RNA sequencing library was prepared following Illumina's TruSeq-stranded-mRNA sample preparation protocol. RNA integrity was checked with Agilent Technologies 2100 Bioanalyzer. Poly(A) tail-containing mRNAs were purified using oligo-(dT) magnetic beads with two rounds of purification. After purification, poly(A) RNA was fragmented using divalent cation buffer at elevated temperature. Quality control analysis and quantification of the

sequencing library were performed using Agilent Technologies 2100 Bioanalyzer High Sensitivity DNA Chip. Paired-ended sequencing was performed on Illumina's NovaSeq 6000 sequencing system (LC Sciences). Data analysis was performed by LC Sciences using Cutadapt and perl scripts to remove the reads that contained adaptor contamination, low quality bases, and undetermined bases. Sequence quality was verified using FastQC and map reads to the genome were performed using HISAT2. To assemble the reads, StringTie was used. Perl scripts and gffcompare were utilized to merge all transcriptomes and reconstruct a comprehensive transcriptome. StringTie and ballgown were used to estimate the expression level of all transcripts.

C57Bl/6 mice (Taconic) at 10-11 weeks old received subcutaneous injections of  $5 \times 10^4$  cells on the right flank with either B16F10 4Ig-B7-H3 cells or B16F10 neg vector cells. Tumors were extracted 38 days after implantation. Cells were digested into a single cell suspension using previously published protocols [136]. Individual cells were captured using the 10x Genomics Chromium Single Cell 3' Library per the manufacturers' protocol and a subsequent cDNA library was generated and sequenced on a NovaSeq6000 S2 sequencer. Data were initially processed and quality controlled using the Cell Ranger Software Pipeline. Cell types were classified based on previously defined cell markers [137]. Data were clustered and dimensionally reduced using UMAP (Uniform Manifold Approximation Projection) utilizing the Seurat R Package [138, 139].

## Statistics

Statistics were calculated using GraphPad Prism 9.0.0 (121). Data are represented as mean  $\pm$  standard error. Pairs were compared using a student's t-test where p-values less than or equal to 0.05 were considered significant.

## Results and Discussion

### Development of a High Affinity, 4Ig-Isoform Selective Antibody for Beta-Radioligand Therapy

To develop a 4Ig-B7-H3-specific antibody with both high affinity to the folded extracellular domain of the human 4Ig isoform and selectivity over the s2Ig isoform, New Zealand White (NZBWF1/J) or Balb/C mice were immunized by foot pad injection with murine L-cells transduced with cassettes expressing human 4Ig-B7-H3 on the cell surface. Host sera were screened by ELISA to assess binding to the extracellular domains of both human 4Ig-B7-H3 and

murine 2Ig-B7-H3, and candidate hybridomas subsequently scaled for further evaluation. Counter-screening was performed for all candidates utilizing live cell fluorescence binding assays to HeLa cells, which are known to express 4Ig-B7-H3 and secrete s2Ig-B7-H3 [53], yielding 3 preliminary antibody candidates that could bind to folded, glycosylated human 4Ig-B7-H3 in the face of s2Ig-B7-H3 *in cellulo*. Final prioritization of leads was ultimately based on high affinity binding by ELISA to folded human 4Ig-B7-H3 (**Figure 1E**). Subsequently, hybridoma expansion was performed to further evaluate murine monoclonal antibody candidate 33B, hereafter known as Molecular Imaging Laboratory 33B (MIL33B), isotype IgG2a, for affinity and specificity against various B7 family members, animal species and isoforms.

Affinity to the folded ectodomain of human 4Ig-B7-H3 in an ELISA format yielded an  $EC_{50}$  of 90.0 pM (95% CI: 62 pM - 130 pM;  $n = 6$ ), substantially higher affinity (18-fold) compared to the plate-bound extracellular domain of murine 2Ig-B7-H3 ( $EC_{50} = 1.7$  nM; 95% CI: 0.47 nM - 5.0 nM;  $n = 6$ ) (**Figure 1D**, **Figure 1S**). Next, MIL33B binding kinetics were measured for folded human, murine and porcine B7-H3 isoforms by biolayer interferometry as a model of binding selectivity between the 4Ig extracellular domain and s2Ig in circulation, resulting in calculated  $K_D$  values of  $7.23 \times 10^{-11}$  M for human 4Ig-B7-H3,  $5.80 \times 10^{-10}$  M for human 2Ig-B7-H3,  $4.11 \times 10^{-8}$  M for mouse 2Ig-B7-H3, and  $1.02 \times 10^{-10}$  M for porcine 4Ig-B7-H3 (**Table 1**, **Figure 1E**, **Figure 2S**). These profiles for MIL33B demonstrated significantly higher affinity for 4Ig-B7-H3 when compared to other B7-H3 antibodies that have been tested clinically, e.g., 8H9 and MGA271 [54-58]. The 8-fold selectivity for the human 4Ig isoform compared to the human 2Ig isoform (**Table 1**, **Figure 1F**) presented MIL33B the opportunity to enhance tumor-targeting by traversing soluble decoy in circulation.

The specificity of MIL33B for B7-H3 versus B7 family members was further evaluated by determination of the affinity of MIL33B to other human and mouse B7 family members and common immune checkpoint proteins.  $K_D$  values by ELISA of MIL33B against plate-bound mouse and human B7-H2, B7-H4, PD-L1, PD-L2, PD-1, and CTLA-4 were not measurable ( $>1 \times 10^{-6}$  M) (**Figure 1E**), yielding  $> 5$  orders of magnitude selectivity. Similarly, biolayer interferometry analysis of the binding of MIL33B to human and mouse B7-H2, B7-H4, B7-H1(PD-L1), PD-L2, and PD-1 were also below the limit of detection demonstrating orders of magnitude of selectivity (**Table 2 and Figure 3S**).

**Table 1. Comparative Affinity and Selectivity of MIL33B to B7-H3 Isoforms.** Biolayer interferometry analysis of MIL33B binding to the extracellular domains of human 4Ig-B7-H3, human 2Ig-B7-H3, mouse 2Ig-B7-H3, and porcine 4Ig-B7-H3. MIL33B demonstrated higher affinity and higher selectivity for the human 4Ig isoform over the 2Ig isoform when compared to other anti-B7-H3 antibodies that have been tested clinically (NR = not reported or calculable). Affinities from other antibodies collected from published values [33, 54, 55, 140, 141]. ADC = antibody-drug conjugate, ADCC = antibody dependent cellular cytotoxicity, UT MDACC = University of Texas MD Anderson Cancer Center, MSKCC = Memorial Sloan Kettering Cancer Center, PUCHI = Peking University Cancer Hospital and Institute.

Antibody	Protein	$K_D$ (M)	$K_D$ Error	Full $R^2$	Affinity ratio: 4Ig to 2Ig
<b>MIL33B</b> Source: UT MDACC Mechanism of Action: RLT & others to be determined	Human 4Ig-B7-H3	7.23E-11	5.96E-12	0.9962	
	Human 2Ig-B7-H3	5.80E-10	5.17E-11	0.9535	8
	Mouse 2Ig-B7-H3	4.11E-08	2.98E-09	0.93	18
	Porcine 4Ig-B7-H3	1.02E-10	1.45E-11	0.99	
<b>Murine 8H9</b> Source: MSKCC, Y-mAbs Therapeutics Mechanism of Action: RLT & inhibition	Human 4Ig-B7-H3	8.90E-09			
	Human 2Ig-B7-H3	8.10E-10			0.09
<b>MGA271</b> Source: MacroGenics Mechanism of Action: RLT, ADCC, CAR-T using scFV	Human 4Ig-B7-H3	9.50E-09			NR
	Human 4Ig-B7H3	1.60E-09			
<b>DS-7300 (Hu-M30)</b> Source: Daiichi Sankyo Mechanism of Action: ADC	Human 4Ig-B7H3	1.60E-08			10.0
	Human 2Ig-B7-H3	1.60E-08			
<b>ABBV-155 (HuAb13v1)</b> Source: AbbVie Mechanism of Action: ADC	Human (isoform not reported)	6.20E-09			NR
	Human 4Ig-B7H3	2.20E-08			NR
<b>MGC018</b> Source: MacroGenics Mechanism of Action: ADC	Human 4Ig-B7H3	2.20E-08			NR
	Human 4Ig-B7-H3	4.5E-9			NR
<b>Affibody-BCH</b> Source: PUCHI Mechanism of Action: RLT	Human 4Ig-B7-H3	4.5E-9			NR
	Human 4Ig-B7-H3	9.9E-10			NR
<b>Hu4G4</b> Source: Soochow University Mechanism of Action: RLT	Human 4Ig-B7-H3	9.9E-10			NR
	Human 4Ig-B7-H3	9.9E-10			NR

**Table 2. MIL33B Affinity to Human and Mouse B7 Immunoglobulin Superfamily Members.** Biolayer interferometry analysis of MIL33B binding to B7-H3 homologues and common immune checkpoint proteins demonstrated no significant affinity, confirming MIL33B specificity for multi-species B7-H3.

Protein	$K_D$ (M)	$K_D$ Error	Full $R^2$
Human PD-L1	> 1.6E-6	N/A	0
Mouse PD-L1	> 1.6E-6	1.15E-07	0
Human PD-1	> 1.6E-6	N/A	0
Mouse PD-1	> 1.6E-6	N/A	0
Human PD-L2	> 1.6E-6	1.24E-08	0
Mouse PD-L2	> 1.6E-6	3.77E-08	0
Human B7-H2	> 1.6E-6	4.52E-09	0
Mouse B7-H2	> 1.6E-6	1.0E-12	0
Human B7-H4	> 1.6E-6	4.19E-09	0
Mouse B7-H4	> 1.6E-6	2.21E-11	0

### Validation of Selective Binding of CDRs of MIL33B to Human Cancers versus Normal Tissues

To evaluate tumor-differentiated binding of B7-H3 by MIL33B, fixed-frozen human tissue arrays

containing microarrayed tissue from multiple organ sites of “normal” or “tumor” tissue were stained using MIL33B labeled with AF594 or the appropriate IgG2a-AF594 labeled control antibody. Differential and tumor-specific binding was observed using MIL33B-AF594 for several tumor types including ovarian, pancreatic, and prostate tumors (Figure 1G).

### Validation of CDR Binding and 4Ig-B7-H3 Protein Targeting by Live Cell Fluorescence Microscopy

To evaluate B7-H3 targeting of MIL33B *in cellulo* (and later *in vivo*), several high and low 4Ig-B7-H3-expressing human and mouse cancer cell lines were generated. By Western blot analysis, parental HeLa cells (HeLa<sup>+/+</sup>) showed relatively high endogenous expression of human 4Ig-B7-H3 and low 2Ig-B7-H3 (Figure 4SA), while a clonal HeLa B7-H3 CRISPR/Cas9 knockout cell line (HeLa<sup>-/-</sup>; KO) showed no detectable protein [59]. As expected, 4T1 (murine triple negative breast cancer), B16F10 (murine melanoma cell lines), and CT26 (murine colon cancer) demonstrated minimal expression of the

murine 2Ig-B7-H3 isoform relative to human tumor cells (**Figure 4SA**). Note that the commercial antibody leveraged in the Western blot experiments likely overestimated the levels of rodent versus human protein as its primary cognate antigen was mouse 2Ig with cross-reactivity to the human protein. To

develop murine lines containing the human 4Ig-isoform of B7-H3, 4T1, B16F10, and CT26 cells were batch transfected with human 4Ig-B7-H3 lentiviral particles, generating cells expressing human 4Ig-B7-H3 protein at levels comparable or less than to those observed in human cancer cells (**Figure 4SA**).

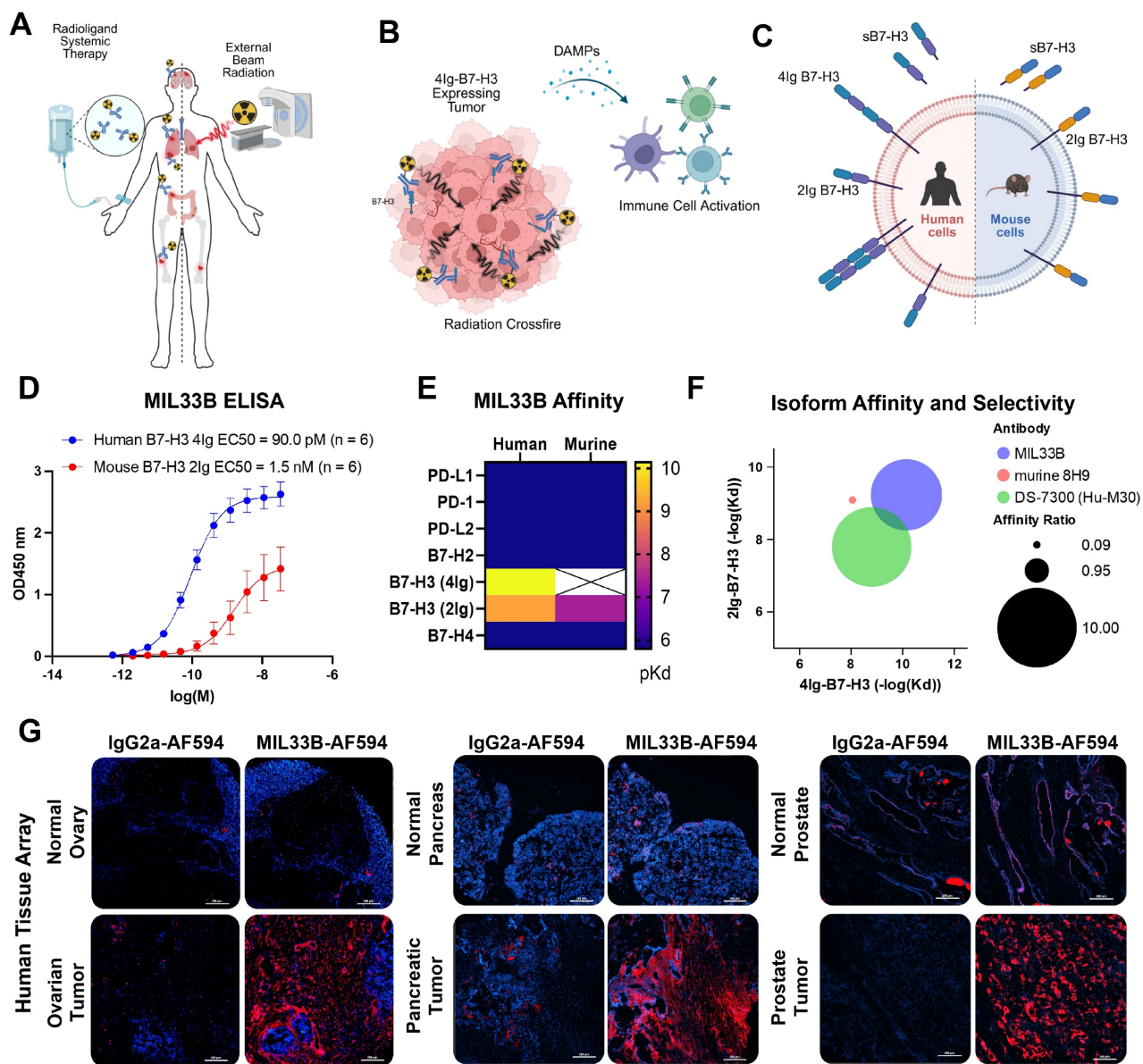


**Figure 1. Development of a high affinity, 4Ig-isoform selective antibody for beta-radioligand therapy.** **A**) Radioligand therapy (RLT) represents systemic therapy whereby the goal is to selectively bind and eliminate primary tumor sites as well as distant metastases and microscopic disease by delivering molecularly-targeted radioactivity through a single therapeutic intervention as compared to conventional external beam radiation therapy (EBRT) which targets with curative intent a defined radiation field localized to the primary tumor, and in some applications, to oligometastatic disease. **B**) Schematic describing the role of “Crossfire” whereby utilizing a 4Ig-B7-H3 molecularly targeted beta-radioligand therapy, the longer distance of the beta-particle deposition and the heterogenous expression of 4Ig-B7-H3 on the tumor and tumor microenvironment allow for a larger, yet still targeted deposition of radiation. Upon damage and tumor cell killing, damage-associated molecular patterns (DAMPs) may be released and provide immune priming signals. **C**) B7-H3 (CD276) is a type-I transmembrane immune modulatory protein with two isoforms found in humans (4Ig-B7-H3 and 2Ig-B7-H3) and a single isoform found in mice (2Ig-B7-H3). There is a soluble 2Ig-component that can be found in circulation, which may serve as a “sink” for non-differentiated isoform-specific anti-B7-H3 antibodies. **D**) ELISA of serial dilutions of MIL33B from different production lots demonstrated high affinity to plate-bound extracellular domain of human 4Ig-B7-H3 (EC50 = 90.0 pM, 95% CI: 62 pM – 130 pM; n = 6), and lower affinity to plate-bound extracellular domain of mouse 2Ig-B7-H3 (EC50 = 1.7 nM, 95% CI: 0.47 nM – 5.0 nM; n = 6). **E**) Heatmap of biolayer interferometry analysis of MIL33B binding to B7-H3 homologues and common immune checkpoint proteins. MIL33B had the highest affinity for human 4Ig-B7-H3 and selection over the 2Ig-B7-H3 human isoform. **F**) MIL33B demonstrated greater isoform affinity and selectivity compared to other anti-B7-H3 antibodies. **G**) Immunofluorescence staining of fresh frozen human tissue microarrays with normal and paired tumor tissue. Images represent IgG2a-AF594 labeled isotype control (left, red) and MIL33B-AF594 (right, red) overlaid on DAPI (nuclear DNA, blue) for normal (top) and cancerous tissue (bottom). Scale bars represent 200  $\mu$ m.

Next, MIL33B binding and specificity for human 4Ig-B7-H3 were tested *in cellulo*. MIL33B and a matched non-targeted isotype control antibody (IgG2a) were labeled with Alexa594. HeLa 4Ig-B7-H3<sup>+/+</sup>, HeLa B7-H3<sup>-/-</sup>, 4T1 4Ig-B7-H3, 4T1 negative vector, B16F10 4Ig-B7-H3, B16F10 negative vector, CT26 4Ig-B7-H3, and CT26 negative vector cells were incubated with either MIL33B-Alexa549, mouse IgG2a-Alexa549, or no antibody. Cell-associated antibody was assessed by live cell fluorescence microscopy, which enabled evaluation of both membrane association and internalization of antibodies over time. MIL33B demonstrated high cell-specific binding to endogenously high 4Ig-B7-H3-expressing human cells (HeLa<sup>+/+</sup>) and cells transduced with human 4Ig-B7-H3 (CT26 4Ig-B7-H3, 4T1 4Ig-B7-H3 and B16F10 4Ig-B7-H3) with a prominent plasma membrane pattern and evidence of internalization by 40 min to 1 h. MIL33B selectivity for 4Ig-B7-H3 versus other tumor surface antigens, FcR binding, and macropinocytosis was demonstrated via the vastly superior binding to cells expressing 4Ig-B7-H3 versus various negative controls, including B7-H3 HeLa KO cells, negative vector control murine cells (reflecting low endogenous murine 2Ig-B7-H3), cells incubated with mouse IgG2a-Alexa549, and autofluorescence of unlabeled cells alone (**Figure 2A-F**, **Figure 4SB-C**). Of note, we observed heterogeneous 4Ig-B7-H3-specific cell labeling of MIL33B in murine cell lines transduced with human 4Ig-B7-H3, consistent with expectations for cells not clonally selected for high 4Ig-B7-H3 expression after transfection. Further specificity of MIL33B versus non-specific membrane adhesion and macropinocytosis was independently validated by pre-incubating HeLa cells with excess un-labeled MIL33B, which blocked MIL33B-Alexa549 binding as assessed by live cell fluorescence microscopy (**Figure 2B**). In addition, because the MIL33B isotype was mouse IgG2a, which has high affinity to mouse FcγR [60], additional validation of specificity versus FcγR binding was evaluated. Indeed, MIL33B pre-blocking was far superior to IgG2a pre-blocking, indicating no substantial Fc-mediated binding to solid tumor-expressed Fc receptors, consistent with the previously demonstrated superiority of MIL33B-AF594 compared to murine IgG2a-AF594 live cell binding and retention (**Figure 1C**). Overall, MIL33B showed high specificity for human 4Ig-B7-H3 protein versus other tumor antigens, tumor expression of FcγR, non-selective membrane binding, and macropinocytosis *in cellulo*.

## Evaluation of MIL33B Targeting Tumor Cell 4Ig-B7-H3 Protein *In Vivo* and Application to Immuno-PET

Next, to determine if MIL33B could be utilized as an effective 4Ig-B7-H3 targeting antibody *in vivo* and demonstrate utility for radio-immuno PET applications, <sup>89</sup>Zr-DFO conjugates of MIL33B and isotype control (<sup>89</sup>Zr-DFO-MIL33B and <sup>89</sup>Zr-DFO-IgG2a, respectively) were generated and characterized. Live animal PET imaging allowed characterization of tumor-specific net retention, kinetics, and whole body biodistribution of MIL33B in different tumor models, and relative organ-specific clearance over time. Zirconium-89 was selected to exploit the long isotope half-life (3.3 days), which both aligned with the long half-life of circulating antibodies *in vivo* and provided ample time to conduct longitudinal imaging of mice injected with each radiolabeled antibody. Similar antibody conjugates have also been translated into humans for various PET applications [61].

To synthesize <sup>89</sup>Zr-DFO-MIL33B and <sup>89</sup>Zr-DFO-IgG2a, each antibody was first conjugated to the chelator DFO (**Figure 5SA**). LC/MS analysis of DFO-MIL33B and DFO-IgG2a identified a mass shift consistent with the addition of two DFO chelators on average per antibody (**Figure 5SD**, **5SG**). Subsequently, DFO-MIL33B and DFO-IgG2a were labeled with <sup>89</sup>Zr-oxalate, purified on a PD-10 column, and characterized by radio-TLC and radio-SEC-HPLC. <sup>89</sup>Zr-DFO-MIL33B labeled with 62.7% ± 13.7% (n = 4) chelation efficiency as measured by radio-TLC. Radio-SEC-HPLC of <sup>89</sup>Zr-DFO-MIL33B immediately after purification demonstrated 82% purity and specific activity of 16.6 μCi/μg (6.14 × 10<sup>4</sup> GBq/μg) (n = 1) (**Figure 5SB-C**). <sup>89</sup>Zr-DFO-IgG2a labeled with 54.5% ± 14.2% (n = 4) chelation efficiency as measured by radio-TLC. Radio-SEC-HPLC of <sup>89</sup>Zr-DFO-IgG2a immediately after purification demonstrated 87% purity and specific activity of 10 μCi/μg (3.7 × 10<sup>4</sup> GBq/μg) (n = 1) (**Figure 5SE-F**).

After intravenous injection of either <sup>89</sup>Zr-DFO-MIL33B or <sup>89</sup>Zr-DFO-IgG2a, the biodistribution and 4Ig-B7-H3-specific tumor-targeting in nude mice harboring either HeLa 4Ig-B7-H3<sup>+/+</sup> tumors or HeLa B7-H3<sup>-/-</sup> tumors were evaluated by PET-CT at 24, 72, and 144 hours post injection. Furthermore, to evaluate the displaceability of <sup>89</sup>Zr-DFO-MIL33B *in vivo*, some mice received 200 μg i.v. of non-radiolabeled MIL33B (cold block) 1 h before receiving <sup>89</sup>Zr-DFO-MIL33B.

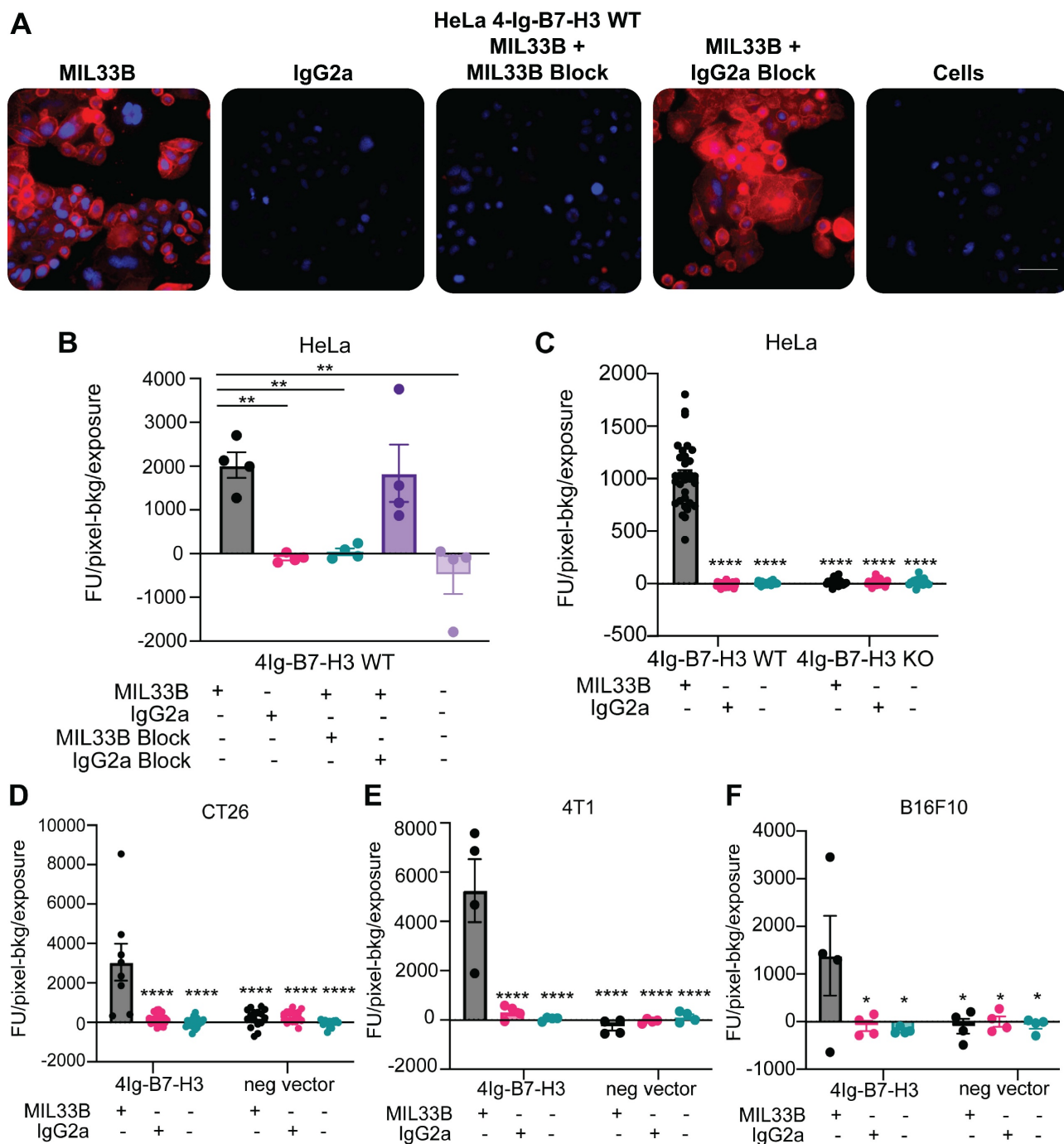


**Figure 2. MIL33B has high affinity and specificity for the human 4lg-B7-H3 isoform. A.** Immunofluorescence live-cell staining of multiple 4lg-B7-H3 expressing cell lines demonstrated 4lg-B7-H3 specific binding and membrane localization of MIL33B. High endogenous 4lg-B7-H3-expressing human HeLa cells incubated with Alexa549-labeled MIL33B demonstrated high intensity membrane-specific localization compared to Alexa549-labeled IgG2a or cells alone when incubated for 1 h. Pre-incubation with un-labeled MIL33B was superior to murine IgG2a in displacing Alexa549-labeled MIL33B (cold block). Scale bar = 100  $\mu$ m **B-F.** Quantification of MIL33B-AF594 or IgG2a-AF594 staining intensity (Fluorescence Units-Background/Seconds of the entire field) following 1 hour incubation with antibodies at 37°C and 5% CO<sub>2</sub> humidity. HeLa WT (**B**), HeLa WT and KO (**C**), CT26 (**D**), 4T1 (**E**), or B16F10 (**F**) were cultured under normal conditions.

HeLa cells were again selected as a key test case because they endogenously express 4lg-B7-H3, secrete s2IgB7-H3, and are infiltrated in the murine immune environment *in vivo* with MDSCs expressing Fc $\gamma$ R [62, 63]. <sup>89</sup>Zr-DFO-MIL33B binding in the tumor compartment in mice harboring HeLa 4lg-B7-H3<sup>+/+</sup> tumors (4.27  $\pm$  1.28 %ID/cc at 24 hours, 5.37  $\pm$  1.40

%ID/cc at 72 hours, and 5.02  $\pm$  1.30 %ID/cc at 144 hours post tracer injection; n = 3) was greater at all timepoints compared to mice harboring HeLa B7-H3<sup>-/-</sup> tumors (1.77  $\pm$  0.63 %ID/cc at 24 hours, 1.69  $\pm$  0.68 %ID/cc at 72 hours, and 1.67  $\pm$  0.61 %ID/cc at 144 hours post tracer injection; n = 3) (**Figure S6A-D**). Note that both <sup>89</sup>Zr-DFO-isotope control and

pre-blocking experiments exhibited significantly different blood pool clearance times, necessitating individualized normalization to blood pool to test for 4Ig-B7-H3-specific tumor retention. To achieve this, organ and tumor activity (%ID/cc; SUV equivalent) was normalized to the blood pool activity (SUV heart) and expressed as organ to heart ratios (SUVR). Herein, blood normalized tumor retention in HeLa 4Ig-B7-H3<sup>+/+</sup> tumors imaged with <sup>89</sup>Zr-DFO-MIL33B ( $3.25 \pm 0.65$ ;  $n = 3$ ) was significantly higher compared to HeLa B7-H3<sup>-/-</sup> tumors ( $0.79 \pm 0.13$ ;  $n = 3$ ; \*  $p = 0.0201$ , un-paired two-tailed t-test), HeLa B7-H3<sup>+/+</sup> tumors imaged with <sup>89</sup>Zr-DFO-MIL33B after pre-blocking with cold MIL33B ( $1.02 \pm 0.18$ ;  $n = 3$ ; \*  $p = 0.0292$ , un-paired two-tailed t-test), HeLa 4Ig-B7-H3<sup>+/+</sup> tumors imaged with <sup>89</sup>Zr-DFO-IgG2a ( $0.77 \pm 0.15$ ;  $n = 3$ ; \*  $p = 0.0201$ , un-paired two-tailed t-test), or HeLa B7-H3<sup>-/-</sup> tumors imaged with <sup>89</sup>Zr-DFO-IgG2a ( $0.67 \pm 0.13$ ;  $n = 3$ ; \*  $p = 0.0173$ , un-paired two-tailed t-test) (**Figure 3A, 3C**). In 4Ig-B7-H3-expressing tumors, tumor activity increased over 24 - 144 hours, whereas the blood pool and other organs showed tracer washout over time (**Figure S7A, 7SC**). Tumor sizes for HeLa 4Ig-B7-H3<sup>+/+</sup> tumors imaged with <sup>89</sup>Zr-DFO-MIL33B ranged from  $32 \text{ mm}^3 - 275.7 \text{ mm}^3$  (mean:  $159.7 \text{ mm}^3$  SD  $\pm 122.3 \text{ mm}^3$ ), compared to HeLa 4Ig-B7-H3<sup>-/-</sup> tumors, which ranged from  $92.26 \text{ mm}^3 - 453.63 \text{ mm}^3$  (mean:  $273.8 \text{ mm}^3$  SD  $\pm 180.7 \text{ mm}^3$ ) (**Figure S7**). Tumor retention of <sup>89</sup>Zr-DFO-MIL33B did not correlate with tumor size (**Figure S7D**). These results demonstrated that <sup>89</sup>Zr-DFO-MIL33B was specific for human 4Ig-B7-H3 in the tumor compartment *in vivo* versus normal tissues or other tumor antigens and demonstrated the requirement for 4Ig-B7-H3 antigen-specific CDRs for tumor retention.

Robustness was further validated by testing 4Ig-B7-H3-expressing 4T1, CT26, and B16F10 syngeneic tumor models. These tumors represent two highly immune infiltrated models and one “immune desert” model (B16F10), respectively, and furthermore enabled assessment of targeting across TH1 (C57BL/6) and TH2 (Balb/c) murine backgrounds [64]. Balb/c mice were implanted subcutaneously with 4T1 4Ig-B7-H3 cells on the right flank and 4T1 negative vector cells on the left flank, and subsequently injected i.v. with either <sup>89</sup>Zr-DFO-MIL33B or <sup>89</sup>Zr-DFO-IgG2a prior to imaging by PET-CT at 24, 72, and 144 hours post tracer injection. Similar to the HeLa tumor model, statistically significant greater retention of <sup>89</sup>Zr-DFO-MIL33B was observed in 4T1 4Ig-B7-H3 tumors compared to 4T1 negative vector tumors, or retention of <sup>89</sup>Zr-DFO-IgG2a in 4T1 4Ig-B7-H3 tumors, or <sup>89</sup>Zr-DFO-IgG2a in 4T1 in neg vector tumors

(**Figure S6E-H**). When tumor-specific retention at 72 hours post tracer injection was normalized to blood pool (heart-associated) counts and compared across tumor types and antibodies, significantly higher normalized retention of <sup>89</sup>Zr-DFO-MIL33B in 4T1 4Ig-B7-H3 tumors ( $2.16 \pm 0.19$ ) was observed compared to the retention of <sup>89</sup>Zr-DFO-IgG2a in 4T1 4Ig-B7-H3 tumors ( $0.64 \pm 0.16$ , \*\*  $p = 0.0036$ , un-paired two-tailed t-test) or in 4T1 neg vector tumors ( $1.07 \pm 0.18$ , \*  $p = 0.0135$ , un-paired t-test) (**Figure 3E**). Although a decrease in the average normalized tumor retention of <sup>89</sup>Zr-DFO-MIL33B in 4T1 negative vector tumors was seen compared to 4T1 4Ig-B7-H3 tumors, the effect size was small. Nonetheless, these results demonstrated overall that expression of human 4Ig-B7-H3 in 4T1 tumors significantly increased tumor-specific retention of <sup>89</sup>Zr-DFO-MIL33B *in vivo* relative to isotype control, and CDR-specific binding to the tumor compartment in a highly immune infiltrated environment, replete with FcγR expression and internalizing MDSCs [63, 65].

Next, the biodistribution and tumor specific-retention of <sup>89</sup>Zr-DFO-MIL33B and <sup>89</sup>Zr-DFO-IgG2a in mice harboring B16F10 (immune desert) tumors either transduced with human 4Ig-B7-H3 or transfected with the relevant negative vector control was evaluated. Statistically significant greater tumor retention of <sup>89</sup>Zr-DFO-MIL33B in B16F10 4Ig-B7-H3 tumors was again observed compared to B16F10 negative vector tumors, or tumor retention of <sup>89</sup>Zr-DFO-IgG2a in B16F10 4Ig-B7-H3 tumors or B16F10 negative vector tumors (**Figure S6I-K**). When blood pool normalized, there was significantly higher normalized tumor retention of <sup>89</sup>Zr-DFO-MIL33B in B16F10 4Ig-B7-H3 tumors ( $3.16 \pm 0.30$ ;  $n = 5$ ) compared to B16F10 negative vector tumors ( $1.20 \pm 0.69$ ;  $n = 3$ ; \*\*  $p = 0.0032$ , un-paired two-tailed t-test), retention of <sup>89</sup>Zr-DFO-IgG2a in B16F10 4Ig-B7-H3 tumors ( $0.81 \pm 0.41$ ;  $n = 4$ ; \*\*\*  $p = 0.0003$ , un-paired two-tailed t-test) or in B16F10 neg vector tumors ( $0.89 \pm 0.52$ ;  $n = 3$ ; \*\*  $p = 0.0015$ , un-paired two-tailed t-test). These results demonstrated that expression of human 4Ig-B7-H3 in the B16F10 murine melanoma model significantly increased tumor-specific retention of MIL33B *in vivo* (**Figure 3F**).

Finally, the biodistribution and tumor-specific retention of <sup>89</sup>Zr-DFO-MIL33B and <sup>89</sup>Zr-DFO-IgG2a in the CT26 murine colon cancer model was investigated. Mice were implanted subcutaneously on the right flank with either CT26 4Ig-B7-H3 cells or CT26 negative vector cells and imaged by PET-CT at 24 and 72 hours post tracer injection (i.v.). As before, following blood pool normalization, significantly higher tumor-specific retention of <sup>89</sup>Zr-DFO-MIL33B

was found in CT26 4Ig-B7-H3 tumors ( $3.62 \pm 1.62$ ;  $n = 5$ ) compared to CT26 negative vector tumors ( $1.89 \pm 0.85$ ;  $n = 5$ ;  $*** p < 0.0001$ , un-paired two-tailed t-test), or tumor retention of  $^{89}\text{Zr}$ -DFO-IgG2a in CT26 4Ig-B7-H3 tumors ( $1.59 \pm 0.71$ ;  $n = 5$ ;  $*** p < 0.0001$ , un-paired two-tailed t-test) or in CT26 negative vector

tumors ( $1.32 \pm 0.59$ , tumors;  $n = 5$ ;  $*** p < 0.0001$ , un-paired two-tailed t-test) (**Figure 3B, 3D, Figure S6-7S**). Again, in this model, these results demonstrated that expression of human 4Ig-B7-H3 significantly increased tumor-specific retention of MIL33B *in vivo*.

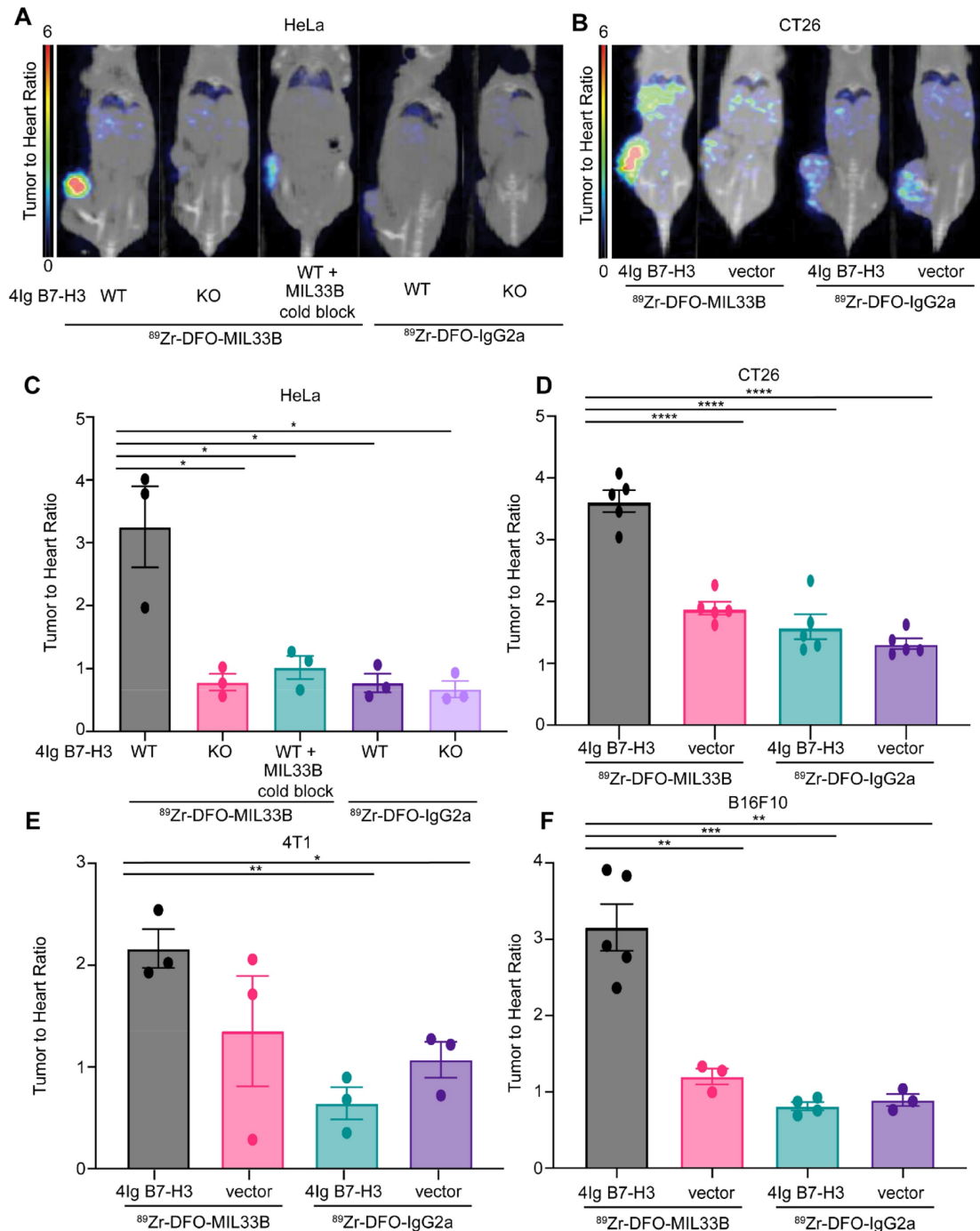


**Figure 3. Immuno-PET demonstrates MIL33B targeting to tumor-specific 4Ig-B7-H3 *in vivo*.** PET/CT images, SUV normalized to heart to correct for animal-to-animal variability in clearance between genotypes for HeLa xenografts (A) and CT26 syngeneic tumor models (B). Images acquired at 72 hours post-injection revealed significantly higher binding and retention of  $^{89}\text{Zr}$ -DFO-MIL33B in mice harboring HeLa B7-H3  $+/+$  tumors compared to HeLa B7-H3  $-/-$  tumors or HeLa B7-H3  $+/+$  tumors pre-treated with cold MIL33B, or HeLa B7-H3  $+/+$  tumors and HeLa B7-H3  $-/-$  tumors imaged with  $^{89}\text{Zr}$ -DFO-IgG2a (A). Similar on-target (B7-H3 expressing tumor) uptake was observed using the syngeneic mouse model for colorectal cancer, CT26 (B). Normalized SUV of  $^{89}\text{Zr}$ -DFO-MIL33B was significantly retained within 4Ig-B7-H3 expressing tumors compared to genotype negative controls or using isotype control,  $^{89}\text{Zr}$ -DFO-IgG2a. The phenotype was observed in four different models including the human cervical cancer cell line, HeLa (C), as well as several murine syngeneic models transfected with human 4Ig-B7-H3 compared to respective tumors transfected with negative vector control or imaged with  $^{89}\text{Zr}$ -DFO-IgG2a; CT26 (D), triple negative breast cancer model 4T1 (E), melanoma model B16F10 (F). Comparisons are determined by un-paired two tailed t-tests, \* $p < 0.05$ , \*\* $p < 0.01$ , \*\*\* $p < 0.001$ .

## MIL33B as a 4Ig-B7-H3-Targeted Radio-Ligand Therapeutic

After validating *in vivo* the 4Ig-B7-H3-specific tumor-targeting properties of MIL33B by PET-CT, MIL33B was engineered into an antibody radio-conjugate for the treatment of solid tumors. Yttrium-90-DOTA conjugates of MIL33B were generated to exploit a beta-emitting radionuclide used clinically in other radio-immunotherapies [66-68] (Figure 1B).

MIL33B was first conjugated to DOTA, followed by chelation of  $^{90}\text{Y}$  (Figure 4A, Figure S8). LC/MS of DOTA-MIL33B was consistent with a mixed pool of one to zero DOTA chelators per antibody (Figure S8C-D). MIL33B-DOTA labeled with  $^{90}\text{Y}$  at greater than  $61.9\% \pm 17.2\%$  ( $n = 4$ ) chelation efficiency as determined by radio-TLC. Radio-SEC-HPLC of purified  $^{90}\text{Y}$ -DOTA-MIL33B demonstrated  $> 99\%$  purity ( $n = 5$ ) and a specific activity of  $3.15 \pm 0.50 \mu\text{Ci}/\mu\text{g}$  ( $1.17 \times 10^{-4} \text{ GBq}/\mu\text{g}$ ) ( $n = 4$ ) (Figure 4B and Figure S8A-B).

## Efficacy of Beta-RLT on 4Ig-B7-H3-Expressing HeLa Tumor Xenografts *In Vivo*

As with fluorescence and  $^{89}\text{Zr}$ -PET imaging, RLT efficacy was first tested with human HeLa xenografts in immunocompromised mice to generate preliminary signals of efficacy in a model that secretes soluble 2Ig-B7-H3 (Figure S9). Mice harboring HeLa 4Ig-B7-H3 $^{+/+}$  tumors ( $n = 10$ ) or mice harboring HeLa B7-H3 $^{-/-}$  KO tumors ( $n = 7$ ) received a single dose (100  $\mu\text{Ci}$ ) of  $^{90}\text{Y}$ -DOTA-MIL33B 30 days after tumor implantation and followed for 120 days (Figure 4C, Figure S10). Compared with untreated animals harboring HeLa WT and KO xenografts (Figure 4D-F), a single dose of  $^{90}\text{Y}$ -DOTA-MIL33B modestly extended median survival for WT B7-H3 expressing tumor xenografts, where the tumors expressed 4Ig-B7-H3 (\*\* $P < 0.001$ , log-rank test; 0.2706, hazard ratio  $^{90}\text{Y}$ -DOTA-MIL33B/no Tx, 95% CI ratio: 0.1140 to 0.6423) (Figure 4D). There was no significant survival benefit for mice harboring B7-H3 KO tumors treated with  $^{90}\text{Y}$ -DOTA-MIL33B, indicating a genotype-specific response (Figure 4E). When all survival curves were superimposed (Figure 4F), the magnitude of response by a single dose RLT can be appreciated wherein  $^{90}\text{Y}$ -DOTA-MIL33B-RLT extended median survival in this immunocompromised model. For a more detailed examination, modified interrupted time series analysis was conducted to compare individual growth rates 15 days before treatment and 15 days after treatment on a per tumor basis. There was a significant decrease in tumor growth rates in treated

HeLa 4Ig-B7-H3 $^{+/+}$  tumors (2-way ANOVA, \*\*  $p = 0.0019$ ) as compared to HeLa B7-H3 $^{-/-}$  KO tumors (2-way ANOVA,  $p = 0.1027$ ) whereby B7-H3 expression on the tumor was knocked out, demonstrating an initial B7-H3-targeted treatment response to  $^{90}\text{Y}$ -DOTA-MIL33B (Figure S10C-D). Note that knockout of B7-H3 in HeLa cells substantially shifts their growth rates compared to wild type cells, the mechanism by which has been dissected by Sutton et. al. [69, 70]. However, compared to short term effects (15 days), substantial long-term differences in overall survival at the end point of paired RLT treatment were not observed (Figure S10A-B). In this immuno-compromised model, an eventual rebound in tumor growth following single dose treatment was observed, consistent with a lack of engagement of the adaptive immune system.

## Efficacy of Beta-RLT in a Syngeneic Tumor Model *In Vivo*

Next, syngeneic immune-competent models of RLT were tested. To fully evaluate the therapeutic efficacy of intravenous  $^{90}\text{Y}$ -DOTA-MIL33B, mouse cohorts harboring established CT26 4Ig-B7-H3 or negative vector tumors were tumor-size selected (50-150  $\text{mm}^3$ ) 10 to 12 days after cell implantation (Figure 4C). Untreated mice were followed regardless of initial tumor size. Based on the results of a pilot dose-response trial, a single dose (100  $\mu\text{Ci}$ ) of  $^{90}\text{Y}$ -DOTA-MIL33B i.v. was characterized in detail for 4Ig-B7-H3-based therapeutic responses. Overall, from a combination of five independent experimental cohorts, 15 mice harboring CT26 4Ig-B7-H3 tumors received  $^{90}\text{Y}$ -DOTA-MIL33B i.v., 9 mice harboring CT26 negative vector tumors received  $^{90}\text{Y}$ -DOTA-MIL33B i.v., 23 mice harboring CT26 4Ig-B7-H3 tumors received an equivalent volume of saline i.v., and 20 mice harboring CT26 4Ig-B7-H3 tumors received no treatment. In the CT26 4Ig-B7-H3 group that received a *single* dose of 100  $\mu\text{Ci}$   $^{90}\text{Y}$ -DOTA-MIL33B i.v., an initial tumor regression of 11 out of 15 tumors was observed; however, 3 tumors emerged at later time points. In the CT26 negative vector group that received 100  $\mu\text{Ci}$   $^{90}\text{Y}$ -DOTA-MIL33B i.v., an initial tumor regression of 2 out of 9 tumors was observed and 1 of these tumors later emerged. In the CT26 4Ig-B7-H3 group that received intravenous saline, tumor regression of only 3 out of 23 tumors was found, and in the CT26 4Ig-B7-H3 groups that did not receive any treatment, spontaneous tumor regression of 1 out of 20 tumors was observed (Figure S11A-D). When mice were followed for 100 days, 53% long-term survivors were observed in mice harboring CT26 4Ig-B7-H3 tumors treated with

$^{90}\text{Y}$ -DOTA-MIL33B i.v., compared to only 11% long-term survivors in mice harboring CT26 negative vector tumors receiving the same dose (\*  $p = 0.0376$ , log-rank test), 13% long-term survivors in mice harboring CT26 4Ig-B7-H3 tumors treated with saline (\*\*  $p = 0.0034$ , log-rank test), and 5% long-term survivors in mice harboring CT26 4Ig-B7-H3 tumors that received no treatment (\*\*\*)  $p = 0.0003$ , log-rank

test) (Figure 4G). When tumors in a subset of animals were harvested at the typical *mid-point* of treatment (day 6-8 post initial  $^{90}\text{Y}$ -DOTA-MIL33B injection), representative tumors from mice harboring CT26 4Ig-B7-H3 tumors treated with  $^{90}\text{Y}$ -DOTA-MIL33B were significantly smaller compared to untreated mice harboring the same tumors (Figure 4H).

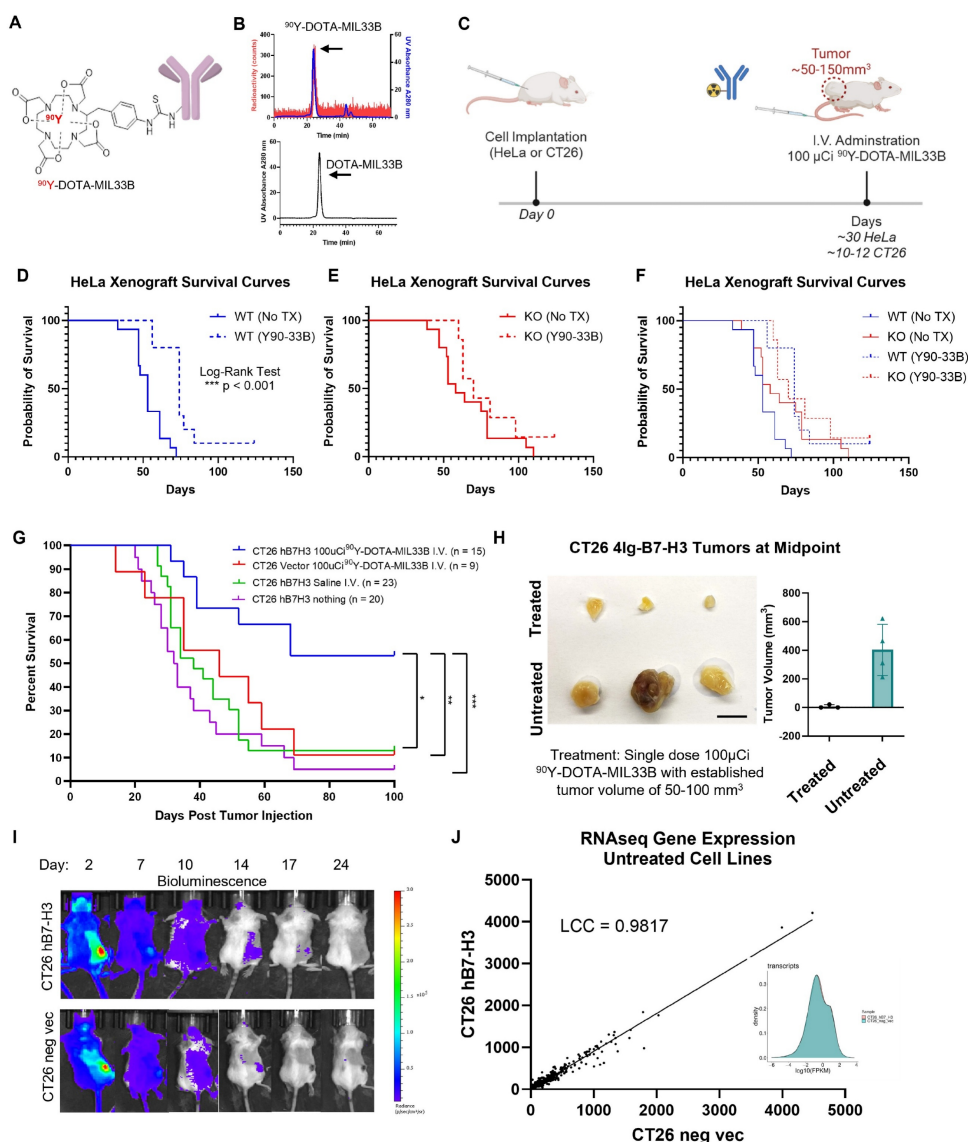


**Figure 4.** Therapeutic efficacy of I.V.  $^{90}\text{Y}$ -DOTA-MIL33B *in vivo*. **A.** Diagram of  $^{90}\text{Y}$ -DOTA-MIL33B. **B.** Radio-HPLC was used to document the labeling efficiency of  $^{90}\text{Y}$ -DOTA-MIL33B. **C.** Experimental schema used for *in vivo* studies to deliver a single dose of 100  $\mu\text{Ci}$   $^{90}\text{Y}$ -DOTA-MIL33B or saline for tumor treatment. **D.**  $5 \times 10^6$  HeLa WT cells were injected into the right flank of athymic nude mice and allowed to establish a tumor for 30 days prior to treatment of half of the mice with  $^{90}\text{Y}$ -DOTA-MIL33B. Survival curves for untreated (solid blue) or treated (dashed blue) were plotted. Single dose treatment with  $^{90}\text{Y}$ -DOTA-MIL33B significantly extended survival \*\*\*  $p < 0.001$ . **E.**  $5 \times 10^6$  HeLa KO cells were injected into the right flank of athymic nude mice and allowed to establish a tumor for 30 days prior to treatment of half of the mice with  $^{90}\text{Y}$ -DOTA-MIL33B. Survival curves for untreated (solid red) or treated (dashed red) were plotted. **F.** Kaplan-Meier survival curves for WT and KO HeLa xenografts were plotted demonstrating the right shift in survival following knockout of B7-H3 from the tumor compartment, and further right shifting with anti-B7-H3 targeted radioligand therapy,  $^{90}\text{Y}$ -DOTA-MIL33B. **G.** CT26 (vector control or h(4Ig)B7-H3 transduced) tumors were implanted subcutaneously in BALB/c mice and allowed to establish a size between 50-100  $\text{mm}^3$  (10-12 days) prior to treatment with saline or a single dose of  $^{90}\text{Y}$ -DOTA-MIL33B (100  $\mu\text{Ci}$ ). Kaplan-Meier survival curves were plotted for CT26-hB7-H3 tumors untreated (purple), CT26-hB7-H3 tumors treated with i.v. saline (green), CT26-vector tumors treated with  $^{90}\text{Y}$ -DOTA-MIL33B (100  $\mu\text{Ci}$ ) (red), and CT26-hB7-H3 tumors treated with  $^{90}\text{Y}$ -DOTA-MIL33B (100  $\mu\text{Ci}$ ) (blue). 4Ig-B7-H3 expressing CT26 tumors treated with a single dose of  $^{90}\text{Y}$ -DOTA-MIL33B (100  $\mu\text{Ci}$ ) had significantly prolonged survival compared to all other treatment groups. **H.** Midpoint tumors collected 7 days post treatment with 100  $\mu\text{Ci}$   $^{90}\text{Y}$ -DOTA-MIL33B for three mice in each group were excised and photographed. Tumor volume for all midpoint tumors was plotted for CT26-hB7-H3 that were treated vs. untreated (N=4 in each group). Scale bar = 1 cm. **I.** Cherenkov imaging of  $^{90}\text{Y}$ -DOTA-MIL33B. Mice harboring CT26 hB7-H3 tumors and CT26-vector tumors were imaged on an IVIS Spectrum 2, 7, 10, 14, 17 and 24 days after I.V. administration of 100  $\mu\text{Ci}$   $^{90}\text{Y}$ -DOTA-MIL33B. Measurement of Cherenkov radiation demonstrated tumor uptake greater in CT26-hB7-H3 than CT26-vector tumors, that diminished overtime. **J.** RNA-sequencing of CT26 4Ig-B7-H3 and CT26 empty vector control cells were performed and gene expression profiles between the cell lines were compared. Gene expression profiles revealed a Lin's Concordance Correlation Coefficient of 0.9817. Density of gene/transcript expression for the two cell lines is presented as density by  $\log_{10}(\text{FPKM})$  (inset).

The low yield positron emission of  $^{90}\text{Y}$  ([71]) is below the threshold for detection by conventional animal PET imaging at the dilute, yet therapeutic, concentrations of  $^{90}\text{Y}$  tested herein [72]. As an alternative to PET imaging, Cherenkov radiation emitted by the beta decay was observed by optical imaging to non-invasively qualify net retention of  $^{90}\text{Y}$ -DOTA-MIL33B in the tumor compartment longitudinally, which confirmed preferential localization of  $^{90}\text{Y}$ -DOTA-MIL33B to 4Ig-B7-H3 tumors versus control tumors *in vivo* (**Figure 4I**), similar to that observed by PET-CT with  $^{89}\text{Zr}$ -labeled MIL33B. Furthermore, white light mode imaging allowed observation of individual tumors over time, confirming complete regression of representative CT26 4Ig-B7-H3 tumors and continued growth of CT26 negative vector tumors (**Figure 4I**). In addition to complete tumor regression, no obvious radiotoxicity was observed in mice that responded to treatment with  $^{90}\text{Y}$ -DOTA-MIL33B (weight, fur, diet consumption, and activity were grossly normal as monitored both by the investigators and impartial veterinary staff). These results demonstrated that a single i.v. injection of  $^{90}\text{Y}$ -DOTA-MIL33B led to complete regression of over half of established CT26 murine colorectal tumors in a 4Ig-B7-H3-dependent manner, demonstrating promise for a high therapeutic index.

To assess the potential impact of 4Ig-B7-H3 neo-antigens as the dominant immune driver, RNA sequencing was performed on the CT26 4Ig-B7-H3 cell line and compared to CT26 empty vector control cells. Gene expression data revealed significantly concordant gene expression profiles (Lin's CCC = 0.9817), with tightly overlapping gene density profiles (**Figure 4J**). Similarly, tumor growth rates and scRNA-Seq data were obtained from untreated B16F10 tumors expressing the exact same empty vector control or human 4Ig-B7-H3 constructs as the CT26 tumors. Overall tumor growth rates were highly correlated, and UMAP plots of 4Ig-B7-H3-expressing B16F10 versus vector control tumors demonstrated strong concordance for the immune cell infiltrates and subtype composition numbers between the two tumor types (**Figure S12**). These data supported the lack of human 4Ig-B7-H3 neo-antigens alone as the dominant immune driver accounting for the response to MIL33B-RLT therapy.

### Non-Radiolabeled (Cold) MIL33B Therapy

As an additional control, MIL33B efficacy as a single agent antibody was explored at a mass in vast excess relative to RLT in a manner consistent with

established immunotherapy regimens for other B7-family targeted anti-cancer therapies. This experiment served as a control to estimate the potential therapeutic contribution of binding of cold MIL33B to human 4Ig-B7-H3, acting either through blockade of B7-H3 signaling pathways, complement, ADCP, or ADCC. Mice implanted with CT26 4Ig-B7-H3 tumors received either 200  $\mu\text{g}$  of MIL33B (non-radiolabeled) i.p., 200  $\mu\text{g}$  of mouse IgG2a isotype control i.p., or PBS i.p., every three days post tumor cell implantation until endpoint (**Figure S13A**), a typical regimen for immune checkpoint therapy in pre-clinical models [73]. Note that immune checkpoint regimens involve substantially higher therapeutic mass of MIL33B (> 32-fold) than the mass used for a single administration of  $^{90}\text{Y}$ -DOTA-MIL33B ( $\leq 50 \mu\text{g}$ ). Compared to  $^{90}\text{Y}$ -DOTA-MIL33B therapy, treatment with cold MIL33B was far inferior, showing no observable effect in this tumor model (**Figure S13A-D**).

### $^{90}\text{Y}$ -DOTA-MIL33B Engages Adaptive Immunity

After establishing that 100  $\mu\text{Ci}$  of  $^{90}\text{Y}$ -DOTA-MIL33B i.v. led to differential regression of established CT26 tumors that expressed human 4Ig-B7-H3 compared to CT26 tumors with low B7-H3 expression, the mechanism of action of this radio-therapeutic response was assessed. First, the composition of the TIME in mice treated with  $^{90}\text{Y}$ -DOTA-MIL33B was characterized by histology. Tumors from mice harboring CT26 4Ig-B7-H3 tumors that had received 100  $\mu\text{Ci}$  of  $^{90}\text{Y}$ -DOTA-MIL33B i.v. were excised at the midpoint of treatment, fixed and saved for histology after radioactive decay (**Figure 5A**). Representative IHC tumor staining for CD3<sup>+</sup>, CD4<sup>+</sup>, and CD8<sup>+</sup> antigens demonstrated positive staining for each of these markers inside the tumor compartment, indicating that CD8<sup>+</sup> and CD4<sup>+</sup> T cells had widely infiltrated into the TIME in mice treated with  $^{90}\text{Y}$ -DOTA-MIL33B i.v. (**Figure 5A**). In addition, the CD3<sup>+</sup>, CD8<sup>+</sup>, and CD4<sup>+</sup> cell populations tended to co-correlate across groups (**Figure S14**).

Having validated antibody binding to tumor-associated 4Ig-B7-H3, mechanistic intervention studies were conducted. Because CD8<sup>+</sup> and CD4<sup>+</sup> T cells were present in the TIME in mice that had previously received 100  $\mu\text{Ci}$  of  $^{90}\text{Y}$ -DOTA-MIL33B i.v., the dependence of treatment response on components of the immune system downstream of the initial radio-ablation was further evaluated. Herein, mice harboring CT26 4Ig-B7-H3 tumors received intravenous treatment with 100  $\mu\text{Ci}$  of  $^{90}\text{Y}$ -DOTA-MIL33B as described previously.

However, one day before treatment, mice received 250  $\mu\text{g}$  i.p. of either anti-CD4- or anti-CD8b-depleting antibodies or the relevant isotype control antibody (anti-rat isotype antibody). Mice subsequently received i.p. injections of depleting antibodies or relevant control antibodies on day 2, day 6, and day 9 post treatment (**Figure 5B**). For mice that received anti-CD4-depleting antibodies, 3 out of 4 tumors initially regressed, but later, 2 of those 3 tumors reemerged. In mice that received anti-CD8b-depleting antibodies, all tumors progressed, and in mice that received anti-rat isotype control antibodies 1 out of 4 tumors regressed (**Figure S15A-C**). When mice were followed for 100 days post tumor implantation, no mice in the group that received anti-CD8b-depleting antibody plus 100  $\mu\text{Ci}$  of  $^{90}\text{Y}$ -DOTA-MIL33B were deemed long-term survivors and these mice reached endpoint faster than mice that received anti-CD4-depleting antibodies plus 100  $\mu\text{Ci}$  of  $^{90}\text{Y}$ -DOTA-MIL33B (25% long-term survivors; \*\*  $p = 0.0091$ , log-rank test). In addition, injections of rat isotype control did not affect the therapeutic efficacy of 100  $\mu\text{Ci}$  of  $^{90}\text{Y}$ -DOTA-MIL33B (25% long-term survivors) (**Figure 5B**). Although relatively smaller sample sizes were used, statistical significance was achieved. Thus, these results indicated that CD8b+-expressing cells, but not CD4+-expressing cells, were necessary to confer long-term therapeutic effects of  $^{90}\text{Y}$ -DOTA-MIL33B *in vivo* and pointed to CD8+ T cells or CD8+ NKT cells as essential contributors to long-term survival.

### Documenting Immunological Memory

While both the HeLa and CT26 models required human 4Ig-B7-H3 in the tumor compartment for beta-RLT to induce an early decrease in tumor volumes, long-term cures were primarily evident in the immune-competent CT26 system. Indeed, there was a correlation between response rate and adaptive immune engagement to produce long-term survivors; nude (nu/nu) mice had 1 long-term survivor whereas syngeneic models that had the ability to engage both innate and adaptive immunity had 8/15 cures. These data and the observed RLT-induced tumor immune infiltrates suggested a potent mechanistic role for cellular adaptive immunity. Thus, to test the potential for cured mice to develop immunological memory as a result of MIL33B-RLT treatment, mice harboring CT26 4Ig-B7-H3 tumors previously treated with 100  $\mu\text{Ci}$  of  $^{90}\text{Y}$ -DOTA-MIL33B and deemed long-term survivors (90 to 110 days post treatment), received a

second re-challenge of fresh CT26 4Ig-B7-H3 cells or CT26 neg vector cells implanted on the left (opposite) flank. Re-challenged mice were compared to naïve mice (age matched; never before inoculated with tumor cells nor treated) also implanted subcutaneously with matched fresh CT26 4Ig-B7-H3 or CT26 negative vector cells on the left flank (**Figure 5C**). Both cohorts were followed for 100 days post tumor cell implantation (200+ days from initial tumor implantation). At study end point, in a combination of two independent experiments, all naïve mice had grown tumors and reached terminal endpoint. Only 1 out of the 5 CT26 4Ig-B7-H3 tumor cell re-challenged mice grew a tumor (\*\*  $p = 0.0035$ , log-rank test); the remaining 4 re-challenged mice were able to fend off tumor re-challenge and survive (**Figure 5C**). Similarly, in the previously treated cohort, 2/3 mice (66%) implanted with CT26 neg vector cells were also able to fend off tumor regrowth. These results indicated that mice with CT26 4Ig-B7-H3 tumors that had previously responded to radio-ligand therapy developed immunological memory, a signature indicating that adaptive immunity was indeed engaged for long-term survival. Additionally, the ability for the re-challenged mice to fend off both CT26-4Ig-B7-H3 and CT26 negative vector tumors suggested that human 4Ig-B7-H3 neo-antigens alone were not the dominant immune driver.

Additionally, multiplexed immunofluorescence staining revealed that many CD4- and CD8-positive immune cells in the TIME of CT26 4Ig-B7-H3 tumors responding to  $^{90}\text{Y}$ -DOTA-MIL33B were also positive for nuclear staining of TCF1/7. The presence of nuclear TCF1/7 staining within CD4+ and CD8+ T-cell populations indicate a stem-like memory phenotype [74], which is critical for sustaining long-term antitumor immunity. Additionally, germinal center structures exhibited dense nuclear TCF1/7 positivity, consistent with active reservoirs of progenitor-like T cells capable of self-renewal and differentiation upon antigen re-exposure (**Figure 5D**). Overall, these findings supported the engagement of durable adaptive immune mechanisms following RLT and the proposed model wherein the effects of  $^{90}\text{Y}$ -DOTA-MIL33B were due to 4Ig-B7-H3-mediated retention of a therapeutic radionuclide, yttrium-90, within the local tumor environment that initiated immunogenic cell death, leading to engagement of innate immunity, an immune priming cascade, and ultimately activation of adaptive immunity (**Figure 5E**).

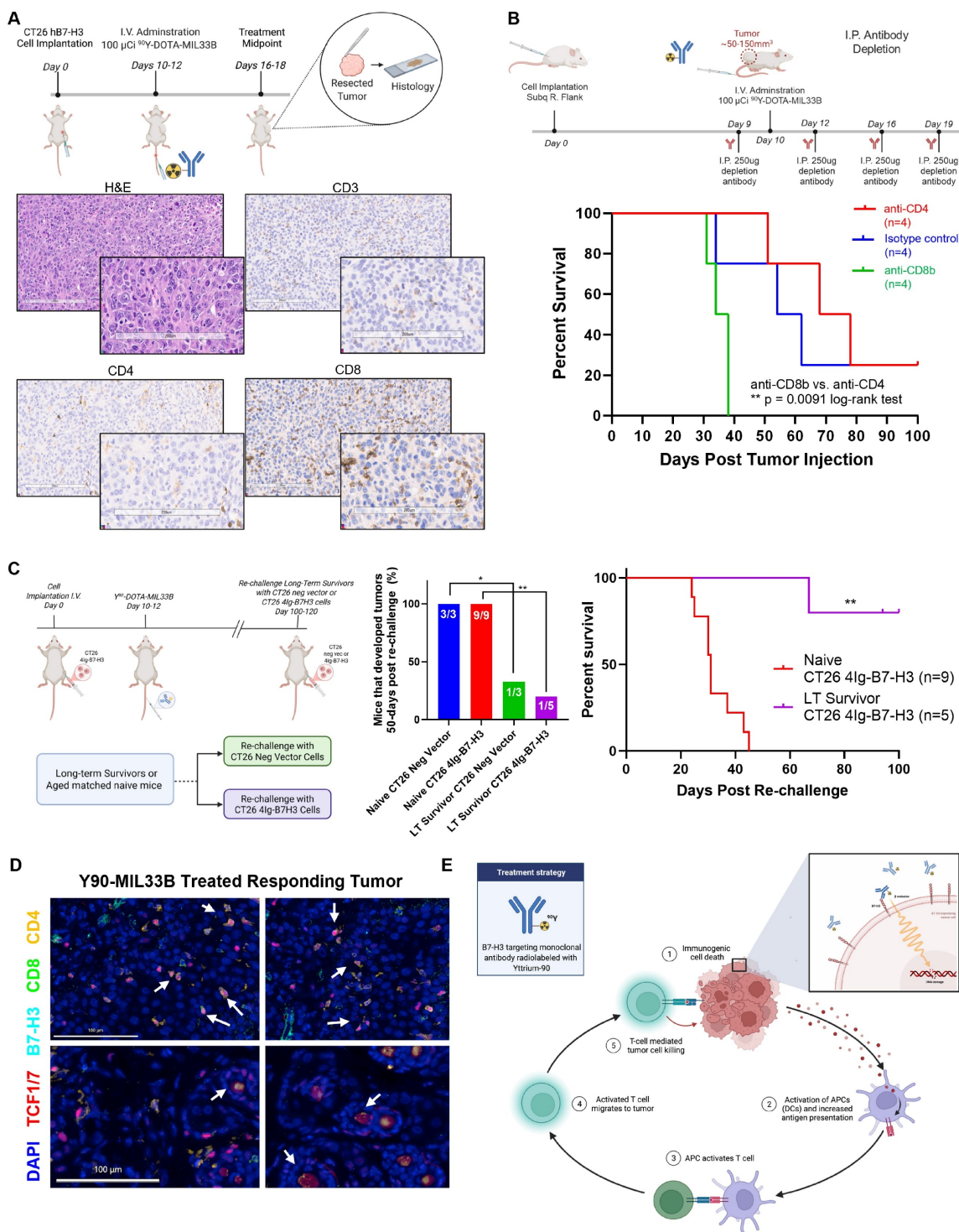


**Figure 5. Treatment with  $^{90}$ Y-DOTA-MIL33B elicits an immunological response.** **A.** Representative histology of a  $^{90}$ Y-DOTA-MIL33B treated tumor. Mice harboring established CT26 hB7-H3 tumors were treated with 100  $\mu$ Ci i.v.  $^{90}$ Y-DOTA-MIL33B. Six days post treatment mice were sacrificed and tumors were fixed in formalin and subsequently stored in 70% ethanol and allowed to decay. Histological staining demonstrated positive CD3, CD4 and CD8 staining in the tumor compartment indicating that both CD4 and CD8 T cells are present. Scale bars represent 200  $\mu$ m. **B.** Immune cell depletion studies identify CD8b cells as essential for  $^{90}$ Y-DOTA-MIL33B response. Mice harboring CT26 4lg-B7-H3 tumors were treated with 100  $\mu$ Ci of  $^{90}$ Y-DOTA-MIL33B i.v. One day before treatment and 2, 4, and 7 days after treatment mice received 250ug I.P. of either anti-CD4 or anti-CD8b depleting antibodies or the relevant isotype control antibody, rat isotype control. Survival curves were compared for isotype control (blue), anti-CD4 (red) and anti-CD8b (green) using the log-rank test. (\*\* =  $p < 0.01$ ). **C.** Re-challenge of  $^{90}$ Y-DOTA-MIL33B i.v. responsive mice. Mice harboring CT26 4lg-B7-H3 tumors that were treated with 100  $\mu$ Ci of  $^{90}$ Y-DOTA-MIL33B i.v. and deemed long-term survivors were re-challenged with CT26 4lg-B7-H3 cells or CT26 neg vector cells on the opposite flank 100-120 days after the initial tumor implantation. 4/5 of CT26 4lg-B7-H3 and 2/3 of CT26 neg vector re-challenged mice rejected the tumors (at day 50 post-rechallenge). In contrast, all naïve mice grew tumors and reached endpoint. Survival curves were compared by the log-rank test (\*\* =  $p < 0.006$ ). **D.** Multiplexed immunofluorescence staining and microscopy of FFPE tissue extracted from a responding CT26 4lg-B7-H3 model that was treated with 100  $\mu$ Ci of  $^{90}$ Y-DOTA-MIL33B i.v. was assessed for the presence of memory immune cells. CD4+ or CD8+ T-cells were identified with nuclear TCF1/7 staining (white arrows). Scale bar = 100  $\mu$ m. **E.** Working model of the immunological response elicited by treatment of CT26-hB7-H3 tumors with  $^{90}$ Y-DOTA-MIL33B beta-radioligand therapy. Beta emissions induce cell damage, leading to immunogenic cell death, release of DAMPs and engagement of innate immunity (1). DAMPs activate APCs (2) leading to increased antigen presentation and activation of T cells (3). T cells then migrate to the tumor (4) and exert additional cytotoxic effects on tumor cells (5).

## Discussion

While B7-H3 expression is generally thought to be “pro-tumor” and immunosuppressive in humans, the detailed signaling functions of the 4Ig and 2Ig isoforms of B7-H3 remain under investigation with both co-stimulatory and co-suppressive immune effects being reported both in cancer and in other inflammatory disorders [40, 75-89]. Indeed, the complexities may be species-specific as rodents have evolutionarily lost the 4Ig isoform. Thus far, non-isoform selective anti-B7-H3 antibody binding or blocking strategies have met with limited clinical success in oncology, particularly relative to anti-B7 therapies targeting the PD-1/PD-L1 axis, although combination anti-B7-H3 therapy with anti-PD-L1 in the context of *PTEN/TP53*-deficiency shows promise in pre-clinical prostate cancer and AML models [90, 91]. Interestingly, soluble ectodomain antigens (in this case, shed ectodomain 2Ig-B7-H3) present challenges to antibody therapy because antibodies bound to antigens are often cleared faster from circulation, altering pharmacokinetics [53, 92, 93]. Furthermore, antibody antigen complexes can lead to off-target toxicities both in the local micro-environment, and in FcγR2-expressing cells [94, 95]. These off-tumor effects can be further compounded in the case of B7-H3 because the concentration of circulating s2Ig-B7-H3 can increase with tumor progression or advanced inflammation, dynamically impacting dosing regimens or potential toxicities [49, 96-100].

Herein, a new high affinity, isoform-selective anti-4Ig-B7-H3 antibody was selected through early use of live cell binding and imaging *in vivo* using strategic models known to present other confounders of binding, including possible tumor-specific glycosylation [101, 102] and dimerization [69, 70]. Through early use of live cell selection,  $B_{\max}$  (the maximum specific binding) in addition to  $K_d$  could be subtly maximized through selection for antibody binding epitopes that are accessible in the context of folded proteins, quaternary structure, and cell surface supramolecular architectures. Isoform-selective anti-4Ig-B7-H3 binding was characterized and validated through biochemical assays *in vitro*, live cell binding and microscopy assays with knockout, knock-in, and blocking studies *in cellulo*, and similarly executed tumor binding and PET-CT imaging studies *in vivo*, which were robust to multiple cell lines, immune-competent and immune-defective murine models, and using both human cells as well as 4Ig-B7-H3 transfected mouse cells. Non-specific membrane adhesion, macro-pinocytosis, B7 paralogues, tumor surface antigens, tumor-expressed FcγR binding, blood accessible murine surface

antigens *in vivo*, FcγR binding *in vivo*, and enhanced permeability-retention (EPR) *in vivo* were tested and demonstrated non-contributory. Finally, through this development process, the platform utility of the antibody for systemic delivery of cargo to 4Ig-B7-H3 compartments *in vivo*, such as the TIME, was demonstrated with PET-CT imaging, Cherenkov imaging, and critically, beta-RLT in a syngeneic CT26 tumor model. Of note, CT26 tumors are characterized as an aggressive MSI-low colorectal carcinoma model radioresistant to conventional external beam radiotherapy [73-75], thus, setting a high bar for pre-clinical advancement of beta-RLT [103-105].

Further analysis of the TIME of CT26 4Ig-B7-H3 tumors at the midpoint of beta-RLT with  $^{90}\text{Y}$ -DOTA-MIL33B revealed that CD4<sup>+</sup> and CD8<sup>+</sup> T cells had infiltrated into the TIME. In addition, mice harboring established CT26 4Ig-B7-H3 whose tumors had previously regressed in response to  $^{90}\text{Y}$ -DOTA-MIL33B developed immunological memory. These phenotypes generally depend upon activation of adaptive immunity. To test this proposed mechanism of immune memory and cure, *in vivo* depletion assays demonstrated that the final therapeutic efficacy of  $^{90}\text{Y}$ -DOTA-MIL33B depended upon CD8b<sup>+</sup>-expressing cells. These results led to a working model wherein the therapeutic effects of  $^{90}\text{Y}$ -DOTA-MIL33B rely on early radiation-induced initiation of immunogenic cell death, activation of innate immunity and antigen presentation, leading to secondary adaptive immune responses and activation of cytotoxic T cells. This is further supported by the early differential response to treatment observed in an immunocompromised tumor model of mice bearing established human HeLa B7-H3<sup>+/+</sup> or HeLa B7-H3<sup>-/-</sup> tumors, wherein treatment with a single dose of  $^{90}\text{Y}$ -DOTA-MIL33B resulted in a significant initial regression of HeLa B7-H3<sup>+/+</sup>-treated tumors superior to HeLa B7-H3<sup>-/-</sup> tumors. In addition, median survival of  $^{90}\text{Y}$ -DOTA-MIL33B-treated HeLa B7-H3<sup>+/+</sup> tumors showed a significant right-shift consistent with a model wherein RLT with  $^{90}\text{Y}$ -DOTA-MIL33B provided an initial immune priming event that could not further engage T-cell mediated immunity in nude mice.

These results point to the general potential of beta-emission-based 4Ig-B7-H3-targeted RLT or radioimmunotherapy as immune priming agents. Previous work has implicated two pathways in radiation-induced activation of the adaption immune system, the release of DAMPs and activation of the cGAS-STING pathway [106, 107]. Both pathways can stimulate antigen presenting cells to present neo-antigens to T cells. Further work with relevant knockout mouse models may pinpoint signaling

pathways activated by  $^{90}\text{Y}$ -DOTA-MIL33B and additional pharmacodynamic biomarkers downstream of target engagement. In this regard, it is interesting to speculate that the cross-fire properties of beta-emitting therapeutic radionuclides such as  $^{90}\text{Y}$  (and  $^{177}\text{Lu}$ ,  $^{67}\text{Cu}$ ) may enhance the repertoire of neoantigens released within the TIME, since both 4Ig-B7-H3-expressing and nearby non-expressing cells will be impacted by local beta emissions, perhaps overcoming intercellular genetic heterogeneity and resistance mechanisms. In addition, although T cells were present in the TIME after treatment with  $^{90}\text{Y}$ -DOTA-MIL33B, it was unknown whether  $^{90}\text{Y}$ -DOTA-MIL33B actively recruited peripheral T cells to the TIME or if  $^{90}\text{Y}$ -DOTA-MIL33B changed the activation setpoint of T cells already residing in the TIME. Discerning this difference may help to further elucidate the mechanism of action of  $^{90}\text{Y}$ -DOTA-MIL33B as well as understand the milieu of the TIME most responsive to RLT. Furthermore, it would be predicted that early disease or micro-metastases will also be impacted by beta-RLT, enabling systemic treatment of metastatic disease, in contrast to EBRT, generally limited to local control of a primary tumor or oligometastatic disease (**Figure 1A-B**).

Development of an isoform-selective anti-4Ig-B7-H3 antibody poses a challenge for use of murine models for characterization of a human-restricted protein target. Mice only express 2Ig-B7-H3, and it could be argued that the effects observed in our study were dominated by human 4Ig-B7-H3 representing a neo-antigen in the context of murine tumor models. However, the ability for the re-challenged mice to fend off both CT26-4Ig-B7-H3 and CT26 neg vector tumors suggested that human 4Ig-B7-H3 neo-antigens were not the dominant immune driver. In addition, tumors treated with non-radioactive MIL33B in a regimen similar to that used with standard immune checkpoint therapies (anti-PD-L1/PD-1; anti-CTLA4), even at much higher “mass” concentrations, showed no significant effect, similar to those treated with IgG2a isotype control antibody or PBS. These data not only provide evidence that MIL33B antibody *per se* was not working in an immune blockade/therapeutic fashion on its own, but highlight that the delivery of beta radioactivity was promoting the observed anti-tumor effect. Finally, using untreated 4Ig-B7-H3-expressing B16F10 tumors versus vector control tumors expressing the same constructs used for all models, scRNA-Seq analysis and UMAP plots demonstrated strong concordance for the identified immune cell infiltrates and numbers of each cell type, further supporting the lack of human 4Ig-B7-H3 neo-antigens

alone as the dominant immune driver.

Clinically, radioembolization with  $^{90}\text{Y}$  in the treatment of hepatic malignancies has previously been shown to increase the CD8<sup>+</sup> T-cell and NKT-cell infiltration into the TIME [108]. Pre-clinically, others have demonstrated that  $^{90}\text{Y}$ -based radionuclide therapy can activate the adaptive immune system in a Non-Hodgkin’s Lymphoma model and synergize with immunotherapy to increase CD8<sup>+</sup> T-cells in the TIME of pre-clinical solid tumor models [109, 110].  $^{90}\text{Y}$ -radio-embolization can elicit an adaptive immune response in humans [108], and human anti-mouse antibody reactions can predict survival after radio-immunotherapy in humans [111-113]. Immune activation downstream of  $^{90}\text{Y}$ -DOTA-MIL33B treatment point to the clinical potential of 4Ig-B7-H3-targeted RLT as both a stand-alone agent and potential immune priming agent for use in combination with other immune checkpoint or immunotherapies for the treatment of many 4Ig-B7-H3-expressing solid and liquid tumors.

B7-H3 is under active exploration as an immune checkpoint, ADC, and CAR T-cell target, and has been previously explored as a radio-immunotherapy target [25, 34-36, 114]. Pre-clinically,  $^{212}\text{Pb}$ -376.96 has been explored for the treatment of human ovarian cancer xenografts and  $^{131}\text{I}$ -4H7 has been investigated in the treatment of human renal cell carcinoma xenografts [115-117]. These pre-clinical studies demonstrated either extended overall survival or tumor growth rate inhibition [115-117]. However, these pre-clinical studies mainly utilized immunodeficient models, and not immunocompetent models, thus curtailing the full range of mechanism of action or resistance to a radio-immunotherapeutics when both the innate and adaptive immune systems are present. 8H9, a murine anti-B7-H3 antibody, is the only anti-B7-H3 RLT that has been investigated clinically [54, 118], focused on non-humanized  $^{131}\text{I}$ -8H9 for the treatment of metastatic neuroblastoma or medulloblastoma by intrathecal injection.  $^{131}\text{I}$ -8H9 and  $^{123}\text{I}$ -8H9 are also under investigation for the treatment of CNS-relapsed rhabdomyosarcoma and DIPG, respectively [119-123]. These trials have yielded promising results in closed CNS compartments [119-123], but attempts at systemic therapy of solid tumors have not been reported, perhaps related to the overall lower affinity of the primary antibody as well as the lack of differential isoform selectivity of 8H9, which has higher affinity for the human 2Ig isoform compared to the 4Ig isoform. The selective 2Ig-B7-H3 affinity may be sufficient when administered in a closed compartment such as the CNS; however, systemic therapy will be substantially hindered by the soluble 2Ig decoy. Similarly, differential uptake was observed

by Fernandes et. al. [114] when comparing two anti-B7-H3 antibodies with differences in isoform affinity, highlighting the importance of understanding both tumor biology and circulating soluble decoys to optimize tumor-specific targeting. This is especially important in the context of systemic RLT, wherein high specific activity radiolabeling methods require use of low masses of antibody (compared to masses of antibody used with immune checkpoint or ADCs). Low mass regime therapeutics, such as RLT, utilizing antibodies with poor selectivity will bind blood decoys, form micro- and macro-immune complexes, remain in circulation or deposit in tissues [124], and thus, deplete the primary antibody, adversely impact pharmacokinetics, and abrogate therapeutic effectiveness. Indeed, soluble decoys may confound many targets relevant to the RLT field, including most B7 family members, as well as PSMA, EGFR, and IGF1R [125-129]. The promise of pre-clearing and pre-targeting strategies used in RLT to manage decoy targets can be a two-edged sword because of immune complex formation [130]. Traversing soluble decoys through engineered antibodies as demonstrated herein provides an alternative and/or complementary strategy.

## Conclusions

In summary, <sup>90</sup>Y-DOTA-MIL33B is an effective radio-ligand therapeutic for the treatment of 4Ig-B7-H3-expressing solid tumors and may have broad potential both as a stand-alone RLT agent and in combination with other immune modulators. Because MIL33B is a high affinity 4Ig-B7-H3-specific targeting agent engineered to traverse soluble (shed ectodomain) s2Ig-B7-H3 *in vivo*, MIL33B provides a modular platform of CDRs and antibody fragments for the delivery of additional therapeutic cargoes, including other beta-emitting and alpha-emitting isotopes, antibody-drug conjugates, peptides, bi- or tri-specific antibodies, and cell-based therapies in oncology. Additional cell-based therapeutics and applications may apply to cardiovascular disease, inflammation, and rheumatological disorders engaging 4Ig-B7-H3, including immune-depletion of memory cells in autoimmunity [131, 132].

## Abbreviations

RLT: Radioligand Therapy  
EBRT : External Beam Radiation Therapy  
ROS: Reactive Oxygen Species  
TIME : Tumor Immune Microenvironment  
PET-CT: Positron Emission Tomography (PET) – Computed Tomography (CT)  
FOV: Field of View

mIF: Multiplexed Immunofluorescence  
UMAP: Uniform Manifold Approximation Projection  
Radio-SEC-HPLC: Radio-Size Exclusion Chromatography-High Pressure Liquid Chromatography  
Bmax: Maximum Specific Binding

## Supplementary Material

Supplementary data, methods, figures and tables.  
<https://www.thno.org/v16p5370s1.pdf>

## Acknowledgements

### Funding Support

Sarah Glazer was supported by an NCI pre-doctoral fellowship (5F30CA239332). Margie Sutton was supported by an NCI post-doctoral fellowship (F32CA250323). The MDACC Small Animal Imaging Facility, Flow Cytometry and Cellular Imaging Core, Research Histology Core Laboratory, and Monoclonal Antibody Facility are supported by a Cancer Center Support Grant (P30 CA016672). Research support was also provided through the University of Texas MD Anderson Cancer Center Quantitative Imaging Analysis Core (QIAC) Partnership in Research (QPR) pilot grant program. We would like to thank members of the Small Animal Imaging Facility (Charles Kingsley, Jorge Delacerda, Emily Newson, and Jennifer Meyer) for their expert assistance with PET-CT imaging, and members of the Monoclonal Antibody Facility (Laura Bover, Felipe Amazy-Manzanares, and Long Vien) for their expert help in developing and producing anti-B7-H3 antibodies. We would also like to extend our gratitude to the members of the Navin Lab and CPRIT SINGLE Core who provided sequencing and consulting for the single-cell RNA-seq analysis performed on murine xenografts (CPRIT SINGLE CORE Facilities Grant (RP180684) and ATGC CORE grants CA016672 (ATGC), NIH 1S10OD024977-01(ATGC)).

### Author Contributions

S.T.G. and D.P.W. designed the antibody immunization and screening strategy. S.E.G, S.T.G and D.P.W designed the *in vitro* and *in cellulo* selection strategy. S.E.G, F.P., S.T.G., and D.P.W. designed radiolabeling and radiotherapy strategies. S.E.G, M.N.S., P.Y., F.P. and S.T.G. designed and executed experiments. All authors provided data analysis. S.E.G, S.T.G., M.N.S, and D.P.W. wrote the manuscript and all authors edited revised manuscripts. D.P.W. provided resources and reagents.

## Data Availability

All source data is contained within the text and Supplemental files or Tables.

## Competing Interests

The University of Texas MD Anderson Cancer Center has filed a patent application on compounds and methods described in this report (S.T.G., F.P. and D.P.W., inventors). The technology is licensed in part to Radiopharm Ventures, LLC. The remaining authors have no conflicts of interest.

## References

- Herrmann K, Schwaiger M, Lewis JS, Solomon SB, McNeil BJ, Baumann M, et al. Radiotheranostics: a roadmap for future development. *Lancet Oncol.* 2020; 21: e146-e56.
- Sgouros G, Bodei L, McDevitt MR, Nedrow JR. Radiopharmaceutical therapy in cancer: clinical advances and challenges. *Nat Rev Drug Discov.* 2020; 19: 589-608.
- Weichselbaum RR, Liang H, Deng L, Fu YX. Radiotherapy and immunotherapy: a beneficial liaison? *Nat Rev Clin Oncol.* 2017; 14: 365-79.
- Kumari S, Mukherjee S, Sinha D, Abdalsalam S, Krishnan S, Asaithamby A. Immunomodulatory Effects of Radiotherapy. *Int J Mol Sci.* 2020; 21(21):8151.
- Liu YP, Zheng CC, Huang YN, He ML, Xu WW, Li B. Molecular mechanisms of chemo- and radiotherapy resistance and the potential implications for cancer treatment. *MedComm (2020).* 2021; 2: 315-40.
- Burgess L, Nguyen E, Tseng CL, Guckenberger M, Lo SS, Zhang B, et al. Practice and principles of stereotactic body radiation therapy for spine and non-spine bone metastases. *Clin Transl Radiat Oncol.* 2024; 45: 100716.
- Maani EV, Maani CV. Radiation Therapy. *StatPearls. Treasure Island (FL) ineligible companies. Disclosure: Christopher Maani declares no relevant financial relationships with ineligible companies.;* 2024.
- Koenig S. Targeting B7-H3 in cancer. *Medicographia.* 2014; 36: 285-92.
- Sun Y, Wang Y, Zhao J, Gu M, Giscombe R, Lefvert AK, et al. B7-H3 and B7-H4 expression in non-small-cell lung cancer. *Lung Cancer.* 2006; 53: 143-51.
- Roth TJ, Sheinin Y, Lohse CM, Kuntz SM, Frigola X, Inman BA, et al. B7-H3 ligand expression by prostate cancer: a novel marker of prognosis and potential target for therapy. *Cancer Res.* 2007; 67: 7893-900.
- Loos M, Hedderich DM, Ottenhausen M, Giese NA, Laschinger M, Esposito I, et al. Expression of the costimulatory molecule B7-H3 is associated with prolonged survival in human pancreatic cancer. *BMC Cancer.* 2009; 9: 463.
- Yamato I, Sho M, Nomi T, Akahori T, Shimada K, Hotta K, et al. Clinical importance of B7-H3 expression in human pancreatic cancer. *Br J Cancer.* 2009; 101: 1709-16.
- Arigami T. B7-H3 ligand expression by primary breast cancer and associated with regional nodal metastasis. *Ann Surg.* 2010; 252: 1044-51.
- Zang X, Sullivan PS, Soslow RA, Waitz R, Reuter VE, Wilton A, et al. Tumor associated endothelial expression of B7-H3 predicts survival in ovarian carcinomas. *Mod Pathol.* 2010; 23: 1104-12.
- Tekle C. B7-H3 contributes to the metastatic capacity of melanoma cells by modulation of known metastasis-associated genes. *Int J Cancer.* 2012; 130: 2282-90.
- Digregorio M, Coppieters N, Lombard A, Lumapat PN, Scholtes F, Rogister B. The expression of B7-H3 isoforms in newly diagnosed glioblastoma and recurrence and their functional role. *Acta Neuropathol Commun.* 2021; 9: 59.
- Greenwald RJ, Freeman GJ, Sharpe AH. The B7 family revisited. *Annu Rev Immunol.* 2005; 23: 515-48.
- Feng R, Chen Y, Liu Y, Zhou Q, Zhang W. The role of B7-H3 in tumors and its potential in clinical application. *Int Immunopharmacol.* 2021; 101: 108153.
- Hau RK, Wright SH, Cherrington NJ. Drug Transporters at the Human Blood-Testis Barrier. *Drug Metab Dispos.* 2023; 51: 560-71.
- Liu L, Liu X. Contributions of Drug Transporters to Blood-Placental Barrier. *Adv Exp Med Biol.* 2019; 1141: 505-48.
- Mulati Y, Shen Q, Tian Y, Chen Y, Yao K, Yu W, et al. Characterizing PSMA heterogeneity in prostate cancer and identifying clinically actionable tumor associated antigens in PSMA negative cases. *Sci Rep.* 2025; 15: 23902.
- Hendriks BS, Klinz SG, Reynolds JG, Espelin CW, Gaddy DF, Wickham TJ. Impact of tumor HER2/ERBB2 expression level on HER2-targeted liposomal doxorubicin-mediated drug delivery: multiple low-affinity interactions lead to a threshold effect. *Mol Cancer Ther.* 2013; 12: 1816-28.
- Kontos F, Michelakos T, Kurokawa T, Sadagopan A, Schwab JH, Ferrone CR, et al. B7-H3: An Attractive Target for Antibody-based Immunotherapy. *Clin Cancer Res.* 2021; 27: 1227-35.
- Moghimi B, Muthugounder S, Jambon S, Tibbetts R, Hung L, Bassiri H, et al. Preclinical assessment of the efficacy and specificity of GD2-B7H3 SynNotch CAR-T in metastatic neuroblastoma. *Nat Commun.* 2021; 12: 511.
- Guo C, Figueiredo I, Gurel B, Neeb A, Seed G, Crespo M, et al. B7-H3 as a Therapeutic Target in Advanced Prostate Cancer. *Eur Urol.* 2023; 83: 224-38.
- Steinberger P, Majdic O, Derdak SV, Pfistershammer K, Kirchberger S, Klauser C, et al. Molecular characterization of human 4Ig-B7-H3, a member of the B7 family with four Ig-like domains. *Journal of immunology (Baltimore, Md : 1950).* 2004; 172: 2352-9.
- Seaman S, Stevens J, Yang MY, Logsdon D, Graff-Cherry C, St Croix B. Genes that distinguish physiological and pathological angiogenesis. *Cancer cell.* 2007; 11: 539-54.
- Xu H, Cheung IY, Guo HF, Cheung NK. MicroRNA miR-29 modulates expression of immunoinhibitory molecule B7-H3: potential implications for immune based therapy of human solid tumors. *Cancer research.* 2009; 69: 6275-81.
- Wang Z-S, Zhong M, Bian Y-H, Mu Y-F, Qin S-L, Yu M-H, et al. MicroRNA-187 inhibits tumor growth and invasion by directly targeting CD276 in colorectal cancer. *Oncotarget.* 2016; 7: 44266-76.
- Wang L, Kang F-B, Sun N, Wang J, Chen W, Li D, et al. The tumor suppressor miR-124 inhibits cell proliferation and invasion by targeting B7-H3 in osteosarcoma. *Tumor Biology.* 2016; 37: 14939-47.
- Yang X, Feng K-X, Li H, Wang L, Xia H. MicroRNA-199a Inhibits Cell Proliferation, Migration, and Invasion and Activates AKT/mTOR Signaling Pathway by Targeting B7-H3 in Cervical Cancer. *Technology in Cancer Research & Treatment.* 2020; 19: 153303382094224.
- Kanchan RK, Perumal N, Atri P, Chirravuri Venkata R, Thapa I, Klinkebiel DL, et al. MiR-1253 exerts tumor-suppressive effects in medulloblastoma via inhibition of CDK6 and CD276 (B7-H3). *Brain Pathology.* 2020; 30: 732-45.
- Benatui L, Bruncko M, Chao D, Izeradjene K, Judd AS, Phillips AC, et al. Anti-b7-h3 antibodies and antibody drug conjugates. In: USPTO, editor. USA: AbbVie; 2017.
- Liang Y, Wu T, Lu Z, Yang X, Du Y, Chen Z, et al. Preclinical evaluation of (89)Zr/(177)Lu-labelled anti-B7-H3 monoclonal antibody for theranostics in B7-H3-positive liver cancer. *Eur J Pharm Sci.* 2025: 107371.
- Xia L, Wu Y, Ren YN, Wang Z, Zhou NN, Zhou WY, et al. A whole-body imaging technique for tumor-specific diagnostics and screening of B7H3-targeted therapies. *J Clin Invest.* 2025; 135.
- Zheng M, Liu QF, Zhang H, Wang YN, Zhang KJ, Mu HW, et al. Development of a Specifically Labeled Zr Antibody for the Noninvasive Imaging of Tumors Overexpressing B7-H3. *Mol Pharmaceut.* 2024; 21: 5205-16.
- Ling V, Wu PW, Spaulding V, Kieleczawa J, Luxenberg D, Carreno BM, et al. Duplication of primate and rodent B7-H3 immunoglobulin V- and C-like domains: divergent history of functional redundancy and exon loss. *Genomics.* 2003; 82: 365-77.
- Sun M, Richards S, Prasad DV, Mai XM, Rudensky A, Dong C. Characterization of mouse and human B7-H3 genes. *Journal of immunology (Baltimore, Md : 1950).* 2002; 168: 6294-7.
- Sun J, Fu F, Gu W, Yan R, Zhang G, Shen Z, et al. Origination of new immunological functions in the costimulatory molecule B7-H3: the role of exon duplication in evolution of the immune system. *PLoS One.* 2011; 6: e24751.
- Chapoval AI, Ni J, Lau JS, Wilcox RA, Flies DB, Liu D, et al. B7-H3: A costimulatory molecule for T cell activation and IFN- $\gamma$  production. *Nature immunology.* 2001; 2: 269-74.
- Hofmeyer KA, Ray A, Zang X. The contrasting role of B7-H3. *Proc Natl Acad Sci U S A.* 2008; 105: 10277-8.
- Khan M, Zhao ZH, Arooj S, Fu YX, Liao GX. Soluble PD-1: Predictive, Prognostic, and Therapeutic Value for Cancer Immunotherapy. *Frontiers in Immunology.* 2020; 11.
- Montemagno C, Hagege A, Borchiellini D, Thamphyha B, Rastoin O, Ambrosetti D, et al. Soluble forms of PD-L1 and PD-1 as prognostic and predictive markers of sunitinib efficacy in patients with metastatic clear cell renal cell carcinoma. *Oncoimmunology.* 2020; 9.
- Liu C, Zhang G, Xiang K, Kim Y, Lavoie RR, Lucien F, et al. Targeting the immune checkpoint B7-H3 for next-generation cancer immunotherapy. *Cancer Immunol Immunother.* 2022; 71: 1549-67.
- Baral A, Ye HX, Jiang PC, Yao Y, Mao Y. B7-H3 and B7-H1 expression in cerebral spinal fluid and tumor tissue correlates with the malignancy grade of glioma patients. *Oncol Lett.* 2014; 8: 1195-201.
- Chen X, Zhang G, Li Y, Feng X, Wan F, Zhang L, et al. Circulating B7-H3(CD276) elevations in cerebrospinal fluid and plasma of children with bacterial meningitis. *J Mol Neurosci.* 2009; 37: 86-94.
- Zhang G, Hou J, Shi J, Yu G, Lu B, Zhang X. Soluble CD276 (B7-H3) is released from monocytes, dendritic cells and activated T cells and is detectable in normal human serum. *Immunology.* 2008; 123: 538-46.
- Xie C, Liu D, Chen Q, Yang C, Wang B, Wu H. Soluble B7-H3 promotes the invasion and metastasis of pancreatic carcinoma cells through the TLR4/NF-kappaB pathway. *Sci Rep.* 2016; 6: 27528.
- Wang L, Kang FB, Zhang GC, Wang J, Xie MF, Zhang YZ. Clinical significance of serum soluble B7-H3 in patients with osteosarcoma. *Cancer Cell Int.* 2018; 18: 115.
- Azuma T, Sato Y, Ohno T, Azuma M, Kume H. Serum soluble B7-H3 is a prognostic marker for patients with non-muscle-invasive bladder cancer. *PLoS One.* 2020; 15: e0243379.
- Avci O, Cavdar E, Iriagac Y, Karaboyun K, Celikkol A, Ozcaglayan TIK, et al. Soluble B7H3 level in breast cancer and its relationship with

- clinicopathological variables and T cell infiltration. *Contemp Oncol (Pozn)*. 2022; 26: 27-31.
52. Wang Z, Yang J, Zhu Y, Zhu Y, Zhang B, Zhou Y. Differential expression of 2lgB7-H3 and 4lgB7-H3 in cancer cell lines and glioma tissues. *Oncol Lett*. 2015; 10: 2204-8.
  53. Tsumagari K, Chang CH, Ishihama Y. Exploring the landscape of ectodomain shedding by quantitative protein terminomics. *iScience*. 2021; 24: 102259.
  54. Ahmed M, Cheng M, Zhao Q, Goldgur Y, Cheal SM, Guo HF, et al. Humanized Affinity-matured Monoclonal Antibody 8H9 Has Potent Antitumor Activity and Binds to FG Loop of Tumor Antigen B7-H3. *J Biol Chem*. 2015; 290: 30018-29.
  55. Loo D, Alderson RF, Chen FZ, Huang L, Zhang W, Gorlatov S, et al. Development of an Fc-enhanced anti-B7-H3 monoclonal antibody with potent antitumor activity. *Clin Cancer Res*. 2012; 18: 3834-45.
  56. Modak S, Guo HF, Humm JL, Smith-Jones PM, Larson SM, Cheung NK. Radioimmunotargeting of human rhabdomyosarcoma using monoclonal antibody 8H9. *Cancer Biother Radiopharm*. 2005; 20: 534-46.
  57. Luther N, Zhou Z, Zanzonico P, Cheung N-K, Humm J, Edgar MA, et al. The potential of theragnostic 124I-8H9 convection-enhanced delivery in diffuse intrinsic pontine glioma. *Neuro-Oncology*. 2014; 16: 800-6.
  58. Aggarwal C, Prawira A, Antonia S, Rahma O, Tolcher A, Cohen RB, et al. Dual checkpoint targeting of B7-H3 and PD-1 with enoblituzumab and pembrolizumab in advanced solid tumors: interim results from a multicenter phase I/II trial. *Journal for ImmunoTherapy of Cancer*. 2022; 10: e004424.
  59. Sutton MN, Glazer SE, Muzzioli R, Yang P, Gammon ST, Piwnica-Worms D. Dimerization of the 4lg isoform of B7-H3 in tumor cells mediates enhanced proliferation and tumorigenic signaling. *Commun Biol*. 2024; 7.
  60. Bruhns P, Jönsson F. Mouse and human FcR effector functions. *Immunol Rev*. 2015; 268: 25-51.
  61. Manafi-Farid R, Ataeinia B, Ranjbar S, Jamshidi Araghi Z, Moradi MM, Pirich C, et al. ImmunoPET: Antibody-Based PET Imaging in Solid Tumors. *Front Med (Lausanne)*. 2022; 9: 916693.
  62. Tzeng A, Kwan BH, Opel CF, Navaratna T, Witttrup KD. Antigen specificity can be irrelevant to immunocytokine efficacy and biodistribution. *Proceedings of the National Academy of Sciences of the United States of America*. 2015; 112: 3320-5.
  63. Wu L, Xu Y, Zhao H, Zhou Y, Chen Y, Yang S, et al. FcγRIIb potentiates differentiation of myeloid-derived suppressor cells to mediate tumor immunoescape. *Theranostics*. 2022; 12: 842-58.
  64. Jovicic N, Jetic L, Jovanovic I, Radosavljevic G, Arsenijevic N, Lukic ML, et al. Differential Immunometabolic Phenotype in Th1 and Th2 Dominant Mouse Strains in Response to High-Fat Feeding. *PLoS One*. 2015; 10: e0134089.
  65. Arlauckas SP, Garris CS, Kohler RH, Kitaoka M, Cuccarese MF, Yang KS, et al. In vivo imaging reveals a tumor-associated macrophage-mediated resistance pathway in anti-PD-1 therapy. *Sci Transl Med*. 2017; 9.
  66. Tong AK, Kao YH, Too CW, Chin KF, Ng DC, Chow PK. Yttrium-90 hepatic radioembolization: clinical review and current techniques in interventional radiology and personalized dosimetry. *Br J Radiol*. 2016; 89: 20150943.
  67. Salem R, Thurston KG. Radioembolization with 90Yttrium microspheres: a state-of-the-art brachytherapy treatment for primary and secondary liver malignancies. Part 1: Technical and methodologic considerations. *J Vasc Interv Radiol*. 2006; 17: 1251-78.
  68. Sharkey RM, Goldenberg DM. Cancer radioimmunotherapy. *Immunotherapy*. 2011; 3: 349-70.
  69. Li L, Li J. Dimerization of Transmembrane Proteins in Cancer Immunotherapy. *Membranes (Basel)*. 2023; 13.
  70. Sutton MN, Glazer SE, Muzzioli R, Yang P, Gammon ST, Piwnica-Worms D. Abstract 6416: Statins inhibit onco-dimerization of 4lg-B7-H3. *Cancer Res*. 2023; 83: 6416-.
  71. Pasciak AS, Bourgeois AC, McKinney JM, Chang TT, Osborne DR, Acuff SN, et al. Radioembolization and the Dynamic Role of (90)Y PET/CT. *Front Oncol*. 2014; 4: 38.
  72. Kao YH, Steinberg JD, Tay YS, Lim GK, Yan J, Townsend DW, et al. Post-radioembolization yttrium-90 PET/CT - part 1: diagnostic reporting. *EJNMMI Res*. 2013; 3: 56.
  73. Liu TW, Gammon ST, Yang P, Ma W, Wang J, Piwnica-Worms D. Inhibition of myeloperoxidase enhances immune checkpoint therapy for melanoma. *J Immunother Cancer*. 2023;11(2):e005837.
  74. Man K, Duarte da Silva VA, Potemkin N, Gabriel SS, Mason T, Elmzazhi T, et al. Stem-like tissue-resident memory T cells control functional heterogeneity and reactivation of T cell memory in the intestine. *Sci Immunol*. 2025; 10: eadw1992.
  75. Zang X, Allison JP. The B7 Family and Cancer Therapy: Costimulation and Coinhibition. *Clinical Cancer Research*. 2007; 13: 5271-9.
  76. Suh WK, Gajewska BU, Okada H, Gronski MA, Bertram EM, Dawicki W, et al. The B7 family member B7-H3 preferentially down-regulates T helper type 1-mediated immune responses. *Nature immunology*. 2003; 4: 899-906.
  77. Loos M, Hedderich DM, Friess H, Kleeff J. B7-h3 and its role in antitumor immunity. *Clin Dev Immunol*. 2010; 2010: 683875.
  78. Nagashima O, Harada N, Usui Y, Yamazaki T, Yagita H, Okumura K, et al. B7-H3 contributes to the development of pathogenic Th2 cells in a murine model of asthma. *Journal of immunology (Baltimore, Md : 1950)*. 2008; 181: 4062-71.
  79. Veenstra RG, Flynn R, Kreymborg K, McDonald-Hyman C, Saha A, Taylor PA, et al. B7-H3 expression in donor T cells and host cells negatively regulates acute graft-versus-host disease lethality. *Blood*. 2015; 125: 3335-46.
  80. Li G, Quan Y, Che F, Wang L. B7-H3 in tumors: friend or foe for tumor immunity? *Cancer Chemother Pharmacol*. 2018; 81: 245-53.
  81. Yonesaka K, Haratani K, Takamura S, Sakai H, Kato R, Takegawa N, et al. B7-H3 Negatively Modulates CTL-Mediated Cancer Immunity. *Clin Cancer Res*. 2018; 24: 2653-64.
  82. Castellanos JR, Purvis JJ, Labak CM, Guda MR, Tsung AJ, Velpula KK, et al. B7-H3 role in the immune landscape of cancer. *Am J Clin Exp Immunol*. 2017; 6: 66-75.
  83. Wang L, Kang FB, Shan BE. B7-H3-mediated tumor immunology: Friend or foe? *Int J Cancer*. 2014; 134: 2764-71.
  84. Mao Y, Chen L, Wang F, Zhu D, Ge X, Hua D, et al. Cancer cell-expressed B7-H3 regulates the differentiation of tumor-associated macrophages in human colorectal carcinoma. *Oncol Lett*. 2017; 14: 6177-83.
  85. Hofmeyer KA, Ray A, Zang X. The contrasting role of B7-H3. *Proceedings of the National Academy of Sciences*. 2008; 105: 10277-8.
  86. Maeda N, Yoshimura K, Yamamoto S, Kuramasu A, Inoue M, Suzuki N, et al. Expression of B7-H3, a potential factor of tumor immune evasion in combination with the number of regulatory T cells, affects against recurrence-free survival in breast cancer patients. *Ann Surg Oncol*. 2014; 21 Suppl 4: S546-54.
  87. Sun X, Vale M, Leung E, Kanwar JR, Gupta R, Krissansen GW. Mouse B7-H3 induces antitumor immunity. *Gene Ther*. 2003; 10: 1728-34.
  88. Prasad DV, Nguyen T, Li Z, Yang Y, Duong J, Wang Y, et al. Murine B7-H3 is a negative regulator of T cells. *Journal of immunology (Baltimore, Md : 1950)*. 2004; 173: 2500-6.
  89. Kreymborg K, Haak S, Murali R, Wei J, Waitz R, Gasteiger G, et al. Ablation of B7-H3 but Not B7-H4 Results in Highly Increased Tumor Burden in a Murine Model of Spontaneous Prostate Cancer. *Cancer Immunol Res*. 2015; 3: 849-54.
  90. Shi W, Wang Y, Zhao Y, Kim JJ, Li H, Meng C, et al. Immune checkpoint B7-H3 is a therapeutic vulnerability in prostate cancer harboring PTEN and TP53 deficiencies. *Sci Transl Med*. 2023; 15: ead6724.
  91. Tyagi A, Ly S, El-Dana F, Yuan B, Jaggupilli A, Grimm S, et al. Evidence supporting a role for the immune checkpoint protein B7-H3 in NK cell-mediated cytotoxicity against AML. *Blood*. 2022; 139: 2782-96.
  92. Stauffer A, Ray C, Hall M. A Flexible Multiplexed Bioanalytical Strategy for Measurement of Total Circulating Shed Target Receptors: Application to Soluble B Cell Maturation Antigen Levels in the Presence of a Bispecific Antibody Drug. *Assay Drug Dev Technol*. 2021; 19: 17-26.
  93. Samineni D, Girish S, Li C. Impact of Shed/Soluble targets on the PK/PD of approved therapeutic monoclonal antibodies. *Expert Rev Clin Pharmacol*. 2016; 9: 1557-69.
  94. James BH, Papakyriacou P, Gardener MJ, Gliddon L, Weston CJ, Lalor PF. The Contribution of Liver Sinusoidal Endothelial Cells to Clearance of Therapeutic Antibody. *Front Physiol*. 2021; 12: 753833.
  95. Rojko JL, Evans MG, Price SA, Han B, Waine G, DeWitte M, et al. Formation, clearance, deposition, pathogenicity, and identification of biopharmaceutical-related immune complexes: review and case studies. *Toxicol Pathol*. 2014; 42: 725-64.
  96. Kovaleva OV, Belova TP, Korotkova EA, Kushlinskii DN, Gratchev AN, Petrikova NA, et al. Soluble B7-H3 in Ovarian Cancer and Its Predictive Value. *Bulletin of Experimental Biology and Medicine*. 2021; 171: 472-4.
  97. Xu Y, Yu L, Hao C, Wang Y, Zhu C, Ji W, et al. Plasma soluble B7-H3 levels for severity evaluation in pediatric patients with *Mycoplasma pneumoniae* pneumonia. *Int Immunopharmacol*. 2019; 73: 163-71.
  98. Chen L, Zhang G, Sheng S, Zhou Q, Pan Y, Guan S. Upregulation of soluble B7-H3 in NSCLC-derived malignant pleural effusion: A potential diagnostic biomarker correlated with NSCLC staging. *Clin Chim Acta*. 2016; 457: 81-5.
  99. Zhang G, Xu Y, Lu X, Huang H, Zhou Y, Lu B, et al. Diagnosis value of serum B7-H3 expression in non-small cell lung cancer. *Lung Cancer*. 2009; 66: 245-9.
  100. Zhang G, Wang J, Kelly J, Gu G, Hou J, Zhou Y, et al. B7-H3 augments the inflammatory response and is associated with human sepsis. *J Immunol*. 2010; 185: 3677-84.
  101. Chen JT, Chen CH, Ku KL, Hsiao M, Chiang CP, Hsu TL, et al. Glycoprotein B7-H3 overexpression and aberrant glycosylation in oral cancer and immune response. *Proc Natl Acad Sci U S A*. 2015; 112: 13057-62.
  102. Huang Y, Zhang HL, Li ZL, Du T, Chen YH, Wang Y, et al. FUT8-mediated aberrant N-glycosylation of B7H3 suppresses the immune response in triple-negative breast cancer. *Nat Commun*. 2021; 12: 2672.
  103. Liu CY, Liao HF, Wang TE, Lin SC, Shih SC, Chang WH, et al. Etoposide sensitizes CT26 colorectal adenocarcinoma to radiation therapy in BALB/c mice. *World J Gastroenterol*. 2005; 11: 4895-8.
  104. Chen B, Alvarado DM, Iticovici M, Kau NS, Park H, Parikh PJ, et al. Interferon-Induced IDO1 Mediates Radiation Resistance and Is a Therapeutic Target in Colorectal Cancer. *Cancer Immunol Res*. 2020; 8: 451-64.
  105. Castle JC, Loewer M, Boegel S, de Graaf J, Bender C, Tadmor AD, et al. Immunomic, genomic and transcriptomic characterization of CT26 colorectal carcinoma. *BMC Genomics*. 2014; 15: 190.
  106. Jagodinsky JC, Morris ZS. Priming and Propagating Anti-tumor Immunity: Focal Hypofractionated Radiation for in Situ Vaccination and Systemic Targeted Radionuclide Theranostics for Immunomodulation of Tumor Microenvironments. *Semin Radiat Oncol*. 2020; 30: 181-6.

107. Zhu M, Yang M, Zhang J, Yin Y, Fan X, Zhang Y, et al. Immunogenic Cell Death Induction by Ionizing Radiation. *Front Immunol.* 2021; 12: 705361.
108. Chew V, Lee YH, Pan L, Nasir NJM, Lim CJ, Chua C, et al. Immune activation underlies a sustained clinical response to Yttrium-90 radioembolisation in hepatocellular carcinoma. *Gut.* 2019; 68: 335-46.
109. Hernandez R, Walker KL, Grudzinski JJ, Aluicio-Sarduy E, Patel R, Zahm CD, et al. 90Y-NM600 targeted radionuclide therapy induces immunologic memory in syngeneic models of T-cell Non-Hodgkin's Lymphoma. *Communications Biology.* 2019; 2.
110. Patel RB, Hernandez R, Carlson P, Grudzinski J, Bates AM, Jagodinsky JC, et al. Low-dose targeted radionuclide therapy renders immunologically cold tumors responsive to immune checkpoint blockade. *Sci Transl Med.* 2021; 13.
111. Azinovic I, DeNardo GL, Lamborn KR, Mirick G, Goldstein D, Bradt BM, et al. Survival benefit associated with human anti-mouse antibody (HAMA) in patients with B-cell malignancies. *Cancer Immunol Immunother.* 2006; 55: 1451-8.
112. Baum RP, Niesen A, Hertel A, Nancy A, Hess H, Donnerstag B, et al. Activating anti-idiotypic human anti-mouse antibodies for immunotherapy of ovarian carcinoma. *Cancer.* 1994; 73: 1121-5.
113. Lamborn KR, DeNardo GL, DeNardo SJ, Goldstein DS, Shen S, Larkin EC, et al. Treatment-related parameters predicting efficacy of Lym-1 radioimmunotherapy in patients with B-lymphocytic malignancies. *Clin Cancer Res.* 1997; 3: 1253-60.
114. Fernandes B, Olkowski CP, Ghaemi B, Basuli F, Shi J, Kiesewetter DO, et al. Unraveling the dynamics of B7-H3-targeting therapeutic antibodies in cancer through PET imaging and antibody pharmacokinetics. *J Control Release.* 2025; 379: 478-88.
115. Wang G, Wu Z, Wang Y, Li X, Zhang G, Hou J. Therapy to target renal cell carcinoma using 131I-labeled B7-H3 monoclonal antibody. *Oncotarget.* 2016; 7: 24888-98.
116. Kasten BB, Arend RC, Katre AA, Kim H, Fan J, Ferrone S, et al. B7-H3-targeted 212Pb radioimmunotherapy of ovarian cancer in preclinical models. *Nuclear Medicine and Biology.* 2017; 47: 23-30.
117. Kasten BB, Gangrade A, Kim H, Fan J, Ferrone S, Ferrone CR, et al. (212)Pb-labeled B7-H3-targeting antibody for pancreatic cancer therapy in mouse models. *Nucl Med Biol.* 2018; 58: 67-73.
118. Modak S, Kramer K, Gultekin SH, Guo HF, Cheung NK. Monoclonal antibody 8H9 targets a novel cell surface antigen expressed by a wide spectrum of human solid tumors. *Cancer research.* 2001; 61: 4048-54.
119. Kramer K, Kushner BH, Modak S, Pandit-Taskar N, Smith-Jones P, Zanzonico P, et al. Compartmental intrathecal radioimmunotherapy: results for treatment for metastatic CNS neuroblastoma. *Journal of Neuro-Oncology.* 2010; 97: 409-18.
120. Kramer K, Pandit-Taskar N, Zanzonico P, Wolden SL, Humm JL, Deselm C, et al. Low incidence of radionecrosis in children treated with conventional radiation therapy and intrathecal radioimmunotherapy. *Journal of Neuro-Oncology.* 2015; 123: 245-9.
121. Ivasyk I, Morgenstern PF, Wembacher-Schroeder E, Souweidane MM. Influence of an intratumoral cyst on drug distribution by convection-enhanced delivery: case report. *Journal of Neurosurgery: Pediatrics.* 2017; 20: 256-60.
122. De B, Kinnaman MD, Wexler LH, Kramer K, Wolden SL. Central nervous system relapse of rhabdomyosarcoma. *Pediatric Blood & Cancer.* 2018; 65: e26710.
123. Souweidane MM, Kramer K, Pandit-Taskar N, Zhou Z, Haque S, Zanzonico P, et al. Convection-enhanced delivery for diffuse intrinsic pontine glioma: a single-centre, dose-escalation, phase 1 trial. *The Lancet Oncology.* 2018; 19: 1040-50.
124. Jancar S, Sanchez Crespo M. Immune complex-mediated tissue injury: a multistep paradigm. *Trends Immunol.* 2005; 26: 48-55.
125. Khan M, Arooj S, Wang H. Soluble B7-CD28 Family Inhibitory Immune Checkpoint Proteins and Anti-Cancer Immunotherapy. *Front Immunol.* 2021; 12: 651634.
126. Machado CML, Skubal M, Haedicke K, Silva FP, Stater EP, Silva T, et al. Membrane-derived particles shed by PSMA-positive cells function as pro-angiogenic stimuli in tumors. *J Control Release.* 2023; 364: 312-25.
127. McElroy B, Powell JC, McCarthy JV. The insulin-like growth factor 1 (IGF-1) receptor is a substrate for gamma-secretase-mediated intramembrane proteolysis. *Biochem Biophys Res Commun.* 2007; 358: 1136-41.
128. McGennis B. HT. Unlocking the potential of PSMA as a cancer target. *MedNouS.* 2020.
129. Wilken JA, Perez-Torres M, Nieves-Alicea R, Cora EM, Christensen TA, Baron AT, et al. Shedding of soluble epidermal growth factor receptor (sEGFR) is mediated by a metalloprotease/fibronectin/integrin axis and inhibited by cetuximab. *Biochemistry.* 2013; 52: 4531-40.
130. Cheal SM, Chung SK, Vaughn BA, Cheung NV, Larson SM. Pretargeting: A Path Forward for Radioimmunotherapy. *J Nucl Med.* 2022; 63: 1302-15.
131. Hashimoto H, Kasteleiner P, Kressin J, Muller F, Buhring HJ, Handgretinger R, et al. Removal of CD276(+) cells from haploidentical memory T-cell grafts significantly lowers the risk of GVHD. *Bone Marrow Transplant.* 2021; 56: 2336-54.
132. Yoon BR, Chung YH, Yoo SJ, Kawara K, Kim J, Yoo IS, et al. Preferential Induction of the T Cell Auxiliary Signaling Molecule B7-H3 on Synovial Monocytes in Rheumatoid Arthritis. *J Biol Chem.* 2016; 291: 4048-57.
133. Muhsin A, Rangel R, Vien L, Bover L. Monoclonal Antibodies Generation: Updates and Protocols on Hybridoma Technology. *Methods Mol Biol.* 2022; 2435: 73-93.
134. Moss BL, Elhammali A, Fowlkes T, Gross S, Vinjamoori A, Contag CH, et al. Interrogation of inhibitor of nuclear factor kappaB alpha/nuclear factor kappaB (IkappaBalpha/NF-kappaB) negative feedback loop dynamics: from single cells to live animals in vivo. *J Biol Chem.* 2012; 287: 31359-70.
135. Zeglis BM, Lewis JS. The bioconjugation and radiosynthesis of 89Zr-DFO-labeled antibodies. *J Vis Exp.* 2015.
136. Bai S. Dissociation of Single Cell Suspensions from Human Breast Tissues. *protocols.io;* 2018.
137. Kumar MP, Du J, Lagoudas G, Jiao Y, Sawyer A, Drummond DC, et al. Analysis of Single-Cell RNA-Seq Identifies Cell-Cell Communication Associated with Tumor Characteristics. *Cell Rep.* 2018; 25: 1458-68 e4.
138. Stuart T, Butler A, Hoffman P, Hafemeister C, Papalexi E, Mauck WM, 3rd, et al. Comprehensive Integration of Single-Cell Data. *Cell.* 2019; 177: 1888-902 e21.
139. Becht E, McInnes L, Healy J, Dutertre CA, Kwok IWH, Ng LG, et al. Dimensionality reduction for visualizing single-cell data using UMAP. *Nat Biotechnol.* 2018.
140. Nagase-Zembutsu A, Hirotani K, Yamato M, Yamaguchi J, Takata T, Yoshida M, et al. Development of DS-5573a: A novel afucosylated mAb directed at B7-H3 with potent antitumor activity. *Cancer Sci.* 2016; 107: 674-81.
141. Scribner JA, Brown JG, Son T, Chiechi M, Li P, Sharma S, et al. Preclinical Development of MGC018, a Duocarmycin-based Antibody-drug Conjugate Targeting B7-H3 for Solid Cancer. *Mol Cancer Ther.* 2020; 19: 2235-44.